Tailorable shielded compliance of thermal barrier coatings through laser texturing and microstructural modification: microfeature design and validation

Artem Bogatyrev [a], Zhirong Liao [a,*], Dragos Axinte [a], Andy Norton [b]

[a] Rolls-Royce UTC in Manufacturing and On-wing Technology, Faculty of Engineering, University of Nottingham, Nottingham NG7 2RD, UK
[b] Rolls-Royce plc, PO Box 31, Derby DE24 8BJ, UK

ABSTRACT

Thermal barrier coatings (TBCs) are widely used for protecting components from an aggressive environment and excessive temperatures. However, the top coat can lack thermal compliance and environmental resistance, promoting premature failure. This study provides an approach to design, produce, and evaluate the novel shielded-compliant TBCs to address these challenges. Top coat laser grooving can lower thermal mismatch levels and hinder crack propagation, whereas laser glazing can enhance strength and anti-corrosion performance. Material analysis for the glazed layer revealed large columnar grains alongside a stress-free structure compared to the as-sprayed coating. The digital image correlation (DIC) in-situ heating test showed vertical cracks after glazing already to be effective stress relief features, with the controlled grooves showing the most prominent compliance, as suggested by finite element analysis (FEA). Such a concept may be applied to any coating where increased thermal compliance or environmental protection is needed, making it a highly versatile tool.

1. Introduction

Thermal barrier coatings (TBCs) play a key role in the safe and efficient operation of components exposed to extreme working conditions, where protection against environmental factors (e.g. oxidation, erosion) and hot gas temperature is needed; as such, a single material component may not be able to survive. These applications include turbine engines (e.g. for use in aircraft and power plants), oil refineries, and recycling units [1]. Such coatings are usually represented by a refractory oxide top coat (TC) layer (e.g. YSZ) and an intermediate bond coat (BC) layer (e.g. NiCoCrAlY) deposited on a superalloy substrate [2]. A fourth layer appears after oxidation of the TBC – a thermally grown oxide (TGO). It is formed in BC at the BC-TC interface and acts as a barrier to prevent further oxidation of BC or substrate. In some cases, TGO may be intentionally created prior to TC deposition to improve BC-TC adhesion, e.g. for electron beam physically vapour deposited (EB-PVD) coatings. As a result, this multilayer system exhibits complex functional behaviour, e.g. mechanical – fracture and wear resistance, thermal insulation, and chemical – oxidation and corrosion protection.

Nevertheless, if the coating fails and delaminates from the substrate, this can lead to catastrophic failure of the whole component, so the coating must be replaced. Thus, increasing the duration between servicing, led by an improvement in the coating cycling life (number of operational heating-cooling cycles before delamination) is of particular interest among academics and industry alike. The community continuously looks for the development of new materials with higher functional performance (e.g. thermal insulation, fracture toughness, corrosion resistance, etc.) while at the same time also investigating improving existing ones. As an example, this may include heat treatment [3–5], nanostructured or functional graded coatings [6–9], doping with different elements [10–12], and segmentation using ribs [13] or cracks [14].

Failure of the coating is governed by a complex interplay of various factors: plasticity, creep, sintering, oxidation, and others, such as calcium-magnesium-aluminium-silicates (CMAS) infiltration and mechanical damage induced by foreign objects [2]. Generalising, the failure modes can be classified as mainly occurring due to high-temperature exposure and the environment.

An aggressive environment (e.g. debris and CMAS) may bring a significant contribution to the TBC failure by mechanical wear and corrosion. To address this, researchers explored densification of the top coat through laser remelting which changes the layer's metallurgical

---

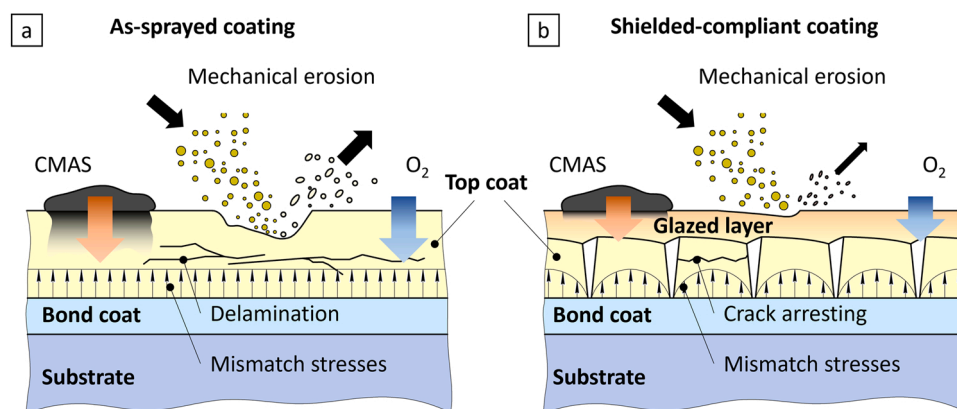**Fig. 1.** Coating before and after modification. (a) As-sprayed coating. (b) Coupled shielded compliance (grooving and glazing) approach. Trenches in the top coat hinder the crack propagation and reduce thermal mismatch stresses, while remelted layer protects from harsh environmental conditions.

structure by increasing the grain size and removing the pores. Yan et al. [15] showed higher corrosion resistance of laser remelted layer against CMAS attack; however, it is noted that CMAS still has some infiltration paths through cracks, which not only damages the as-sprayed top coat but also densifies the glazed layer. Later this issue was addressed by Guo et al. [16], where the coating was glazed twice to bifurcate the vertical crack in the remelted layer to hinder CMAS infiltration paths. At the same time, a notable increase in the microhardness due to densification significantly improves the wear resistance of the coating as was demonstrated by Tsai et al. [17]. Another effect of reducing the porosity is decreased oxygen permeability of the top coat. Zhao et al. [18] showed that this causes retardation of TGO growth rates, which may imply an additional increase in thermal cycling life.

However, these studies do not disclose how the rigidity of such a fully dense layer affects the TBC. Even though the thermal expansion coefficient is not affected by porosity, an increased Young's modulus with creep can result in a massive compressive stress build-up on cooling. This may lead to buckling, which causes spallation of the whole layer. In addition to that, the absence of voids in this layer will increase thermal conductivity affecting the efficiency of the coating's main purpose – thermal insulation.

At the same time, high temperatures cause thermal expansion strains, which will differ across the layers of the TBC system due to different thermal expansion coefficients. As there is no separation between the layers, each of them will develop an additional mechanical strain equalising the total deformation value. This mechanical portion of the strain brings in thermal mismatch stresses which could lead to delamination. Furthermore, exposure to high temperatures causes oxidation of the bond coat with TGO formation. This leads to additional strain due to the volume difference between BC and TGO, and, on cooling this oxide layer can develop compressive stresses down to − 4.5 GPa [19], initiating cracking. The creep and yielding of the bond coat under thermal cycling gradually roughen the BC-TC interface increasing local stresses as well as the risk of failure [20]. Sintering of the top coat makes it more dense and brittle, thus, more susceptible to cracking. Following creep strain relaxation causes compressive stresses to build up on cooling [21], which can drive spallation and buckling. In addition to that, surface undulations of the substrate, needed for good adhesion, cause out-of-plane stresses in the interface which build up on multiple heating-cooling cycles [22].

In this respect, increasing top coat compliance would allow it to accommodate the mechanical portion of the mismatch strain and reduce the stress values. Overall decrease in stresses could promote the improved lifespan of the TBC, as it will reduce creep and yielding effects in the layers. For example, air plasma sprayed (APS) coating is less compliant than EB-PVD, where each whisker is separated and can freely move and expand in the space around it upon heating, which is reflected

on coatings' lifespan. Several attempts were made on increasing the coating's compliance. Dhineshkumar et al. [23] demonstrated that grooving the top coat with a picosecond laser may lead to an increase in thermal cycling life; however, they did not provide a full scientific perspective of the enhancement mechanism. Moreover, there was no investigation into how patterning parameters (width, height, and spacing) influence the result on their own. Later, Khan et al. [24] used a greater variation in grooving parameters and showed a certain parameter set to have the smallest mass loss percentage in the ablation test. However, simultaneous variation of the width and the depth of the trench did not allow for the separation of their influence, and the claimed increase in durability is not presented alongside any reasoning.

Currently, there is no rationale given on how to design such grooving features, leaving this idea in a *craft* state with no scientific basis behind it. Furthermore, the presence of open gaps in the top coat can intensify the hot gas and CMAS propagation, which will alleviate any advantages of increased compliance.

Noteworthy, coating remelting by itself can promote better thermal compliance due to grain morphology transformations. Chen et al. [25] studied the thermal shock behaviour of nanostructured YSZ coatings glazed with a continuous laser. They showed that changing laser scanning speed, which results in a change in the energy density, leads to a considerable variation in the thermal shock durability. An explanation was given in different grain morphology, where columnar grains with intergranular spacing have larger thermal compliance. Similar results were obtained by Fan et al. [26], where the coating experienced an increase in thermal shock life after pulsed laser glazing with columnar structure formation. However, they did not account for the variation in the glazed layer thickness which was a result of different laser scanning speeds.

The as-sprayed coating (Fig. 1, a), having a splat-like structure, can suffer from low compliance, high corrosion, and abrasive wear. In this paper to address both issues, a coupled shielded compliance approach is proposed, including increased compliance alongside environmental resistance. By using a laser, the TBC is segmented by vertical grooves in the top coat, and its outer layer is remelted to achieve a dense glazed structure. Such a modification has the synergising potential of combining the advantages of grooving and glazing on their own: lower thermal mismatch levels, crack arresting and wear resistance. At the same time, it would reduce the drawbacks – providing protection from the hot gas and CMAS, and a compliant base for the glazed layer (Fig. 1, b).

However, it is not known how to design such a system and how to assess it, which is of key importance when it comes to safety-critical components in aerospace. Since the main driving factor here will be stress caused by working at high temperatures, this structure can be designed through thermo-mechanical modelling (e.g. using finite
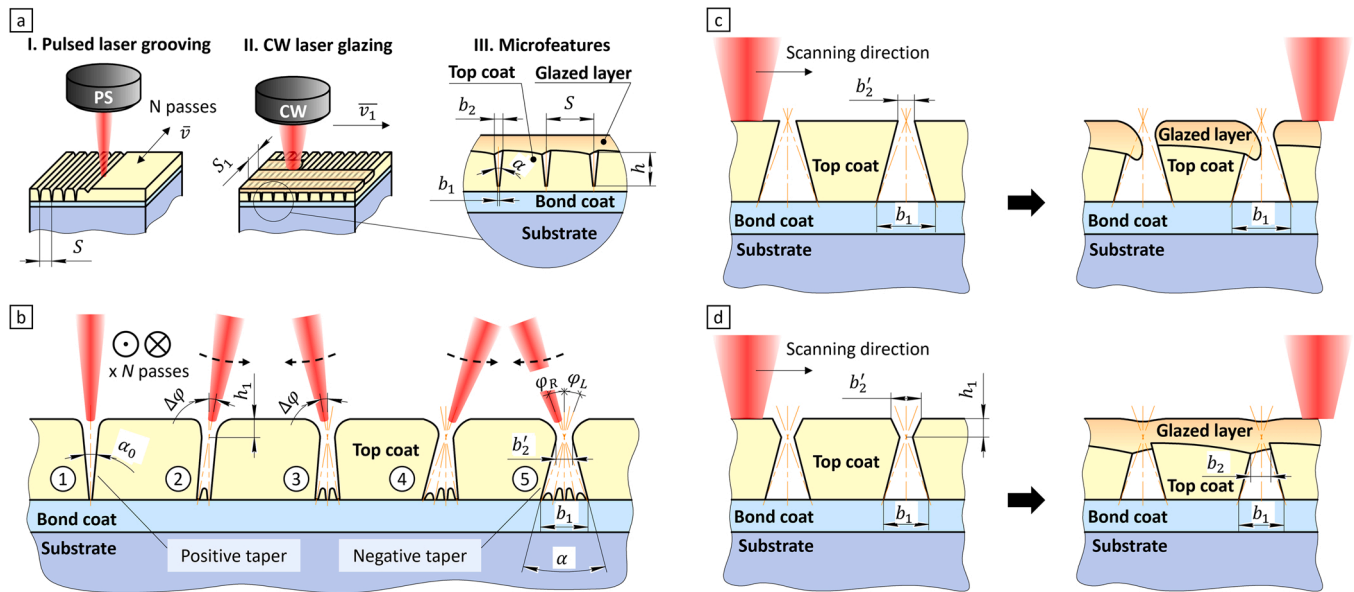
Fig. 2. Grooving and glazing strategy. (a) General shielded compliance modification framework. (b) Pulsed laser ablation of a negatively tapered (dove-tail) groove. The laser machines a single trench per N passes (positively tapered groove) and rotates at a certain angle $\Delta\varphi$, where the process repeats. Rotation continues in a pendulum way until the desired value of right and left profile angles (φ_R, φ_L) is achieved. Final groove angle α is defined by a single trench angle α_0 and the profile angles ($\alpha = \varphi_R + \varphi_L - \alpha_0$). (c) Glazing of dove-tail grooves with a continuous wave laser (no offset). If the intersection point of the groove lies on the surface, even with the opening b_2' being the smallest possible value, remelted material will fall into the groove as it has no support. (d) Glazing of dove-tail grooves with a continuous laser (with offset h_1). Additional offset brings the intersection point below the surface, allowing having some support during glazing, which leads to a continuous glazed layer.

element analysis (FEA)).

In order to reveal how the proposed shielded compliance modification affects the TBC functional behaviour, an in-situ scanning electron microscope (SEM) heating test with digital image correlation (DIC) analysis is introduced. Even though DIC provides only information about strains, this data can be transformed into thermally-induced stresses through Hooke's law. As it was mentioned above, thermally induced stresses governed by the mismatch in thermal expansion coefficients play an important role in affecting the coating's life. Hence, these stresses can be used in a quantitative evaluation of a particular structure (grooves and glazing) at elevated temperatures using DIC analysis. As a case study, these proposals will be applied to samples with the 8%-wt. YSZ APS top coat as a generic example for the presented approach with relevance to the aerospace industry.

2. Shielded compliance modification of TBC: coupled grooving and glazing approach

To improve the thermal and mechanical performance of TBCs, a coupled laser grooving and glazing approach is proposed in this paper to achieve a unique structure. Firstly, the top coat is laser machined to create linear parallel trenches in the as-sprayed material, producing an arrangement of pillars (Fig. 2, a-I). Such pillars mimic the behaviour of the EB-PVD whiskers – the top coat expands in the grooves upon heating and the BC-TC thermal mismatch levels are reduced, which promotes lower stress states under uniform or gradient thermal loads. Moreover, lateral crack propagation is hindered by the presence of grooves (Fig. 1, b); once it achieves a groove's edge, it stops. Thus, delamination will be trapped within single pillars rather than being continuously spread.

At the same time, to eliminate the shortcuts for the hot gas and CMAS propagation the outer layer of the pillars is remelted, in such a way that it bridges the gaps (grooves) and creates a dense continuous layer (Fig. 2, a-II). The increased density and hardness of the glazed layer contribute to the environmental protection of the coating – lower CMAS infiltration rates and reduced mechanical erosion. Furthermore, the altered metallurgical structure with little to no cracks and pores can lead

to increased fracture toughness and strength of the layer, while the elongated columnar grains can additionally increase the compliance level. And the top coat pillars act as compliant supports for the dense rigid glazed layer (Fig. 2, a-III), which on its own would restrain the deformation and promote higher stress states.

Since grooves in TBCs require careful and precise (order of 10 – 100 μm) generation, so as not to damage the underlying bond coat and substrate, laser machining was chosen because of its accuracy and efficiency. It has almost negligible mechanical loads and can be used both for micromachining (grooving) and metallurgical modification (glazing), with only laser systems being changed from pulsed to continuous.

In order to tailor the shielded-compliant structure to specific working conditions of the coated component, it must be revealed how the shape of the groove affects the stress state of the coating. In the simplest case, only the groove spacing S can be varied, however, it will be limited by the pillar's structural strength and providing even heating and flowing conditions for the material during glazing. Even though the periodicity of the grooves may play an important role, it is their cross-section that provides the thermal mismatch relief, and the regularity of the structure (defined by the spacing S) only enhances it.

The groove's geometry can be described by the opening width b_2 and the tip width b_1; or b_2 and the shape angle α at the groove depth h (Fig. 2, a-III). However, during single-cut grooving, these parameters strongly relate to the thermal properties of the material, producing a *positively tapered* groove with $\alpha = \alpha_0$ (Fig. 2, b-1). Variations of the tip width b_1 can be achieved by changing the shape angle α by rotating the sample stage (or the laser beam) while maintaining the relative defocusing distance and position of the laser beam (compucentric rotation). It was discovered, that to achieve a symmetric shape of the groove this rotation must be done in a pendulum way (Fig. 2, b). Nonetheless, even though the opening width b_2 will play a part in stress state alterations of the grooved structure, its variations are limited. If b_2 is too large, the remelt during the glazing stage would not bridge the gap, leaving trenches unprotected from environmental attacks. Such an issue was solved by selecting laser parameters, which provided the smallest b_2 (not covered
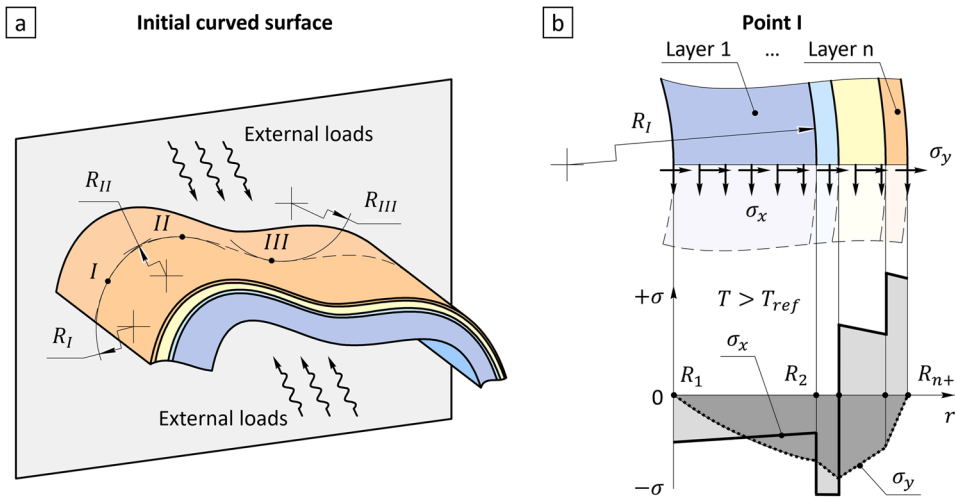
Fig. 3. Schematics to study the influence of curvature and glazing thickness on the stress state of the coating. (a) Multilayered surface with one principal curvature, with external loads acting on the inner and outer surfaces. The sectioning plane defines a curve that can be approximated with arcs (R_I, R_{II}, R_{III}, etc.) at every point. (b) Multilayered hollow cylinder cross-section (only a portion is shown). This cylinder represents only one point of the initial surface of a particular radius (e.g. R_I). In-plane (σ_x) and out-of-plane (σ_y) stresses are calculated across the radius of the cylinder r at temperatures above the reference temperature ($T > T_{ref}$).
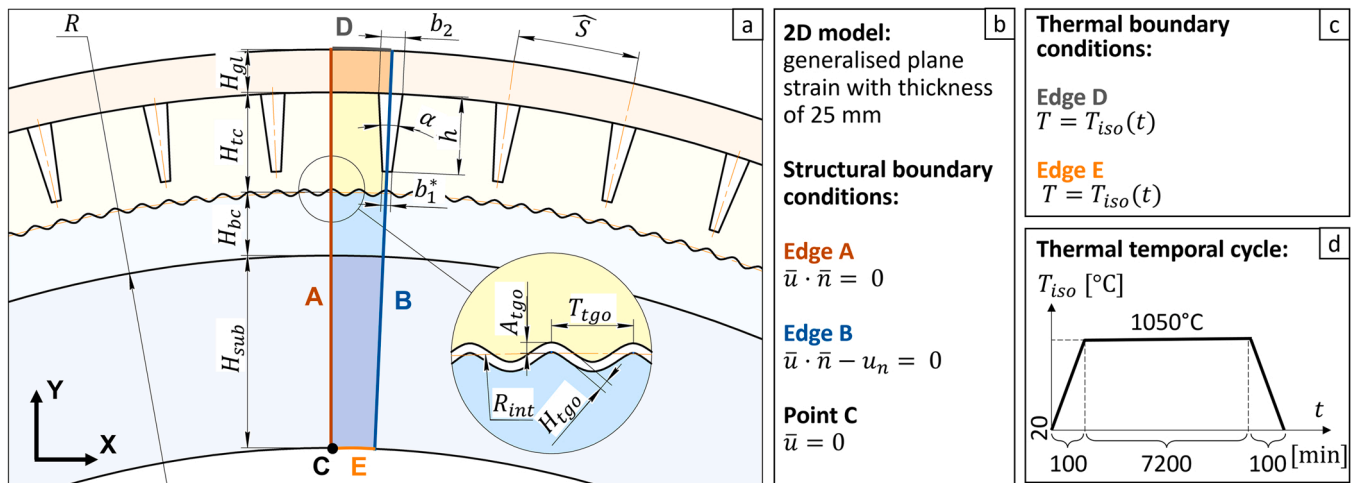
Fig. 4. Geometry and boundary conditions used in the finite element model. (a) Sample geometry, defined as a generic piece of a periodic structure. The curvature of the system is set by substrate surface radius R, and the thicknesses of each layer are H_{sub}, H_{bc}, H_{tgo}, H_{tc}, H_{gl} (substrate, bond coat, thermally grown oxide, top coat, and glazed layer). The groove is defined by an opening width b_2, shape angle α and the height h; the bottom width b_1 is shown for reference. Spacing between the grooves is set as an arc length of the outer diameter (glazed layer) S. (b) Boundary conditions of the structural model (generalised plane strain). (c) Thermal conditions are applied as an isothermal heating-cooling cycle. (d). The temporal thermal cycle, starting with heating, dwelling at the maximum temperature and cooling down to the initial temperature.

in this paper). In the case of grooves with a *negative taper*, i.e. *dove-tail* grooves (Fig. 2, b-5), an additional issue was identified. Due to the wall inclination, during the glazing stage, the material will drop down due to gravitation and will not bridge the gap (Fig. 2, c). However, if to move the laser beam intersection point below the surface of the coating, i.e., to create an offset of about $h_1 = 60$ μm, this problem is solved (Fig. 2, d).

3. Methods

3.1. A modelling approach to designing the novel shielded-compliant structure

3.1.1. Influence of the surface curvature and glazing thickness

Evaluating the stress states in the TBC under thermal loads can help in understanding the modification mechanism. In most cases, the coating is deposited on a non-flat (free-form) surface, e.g. pipes or turbine blades. In this circumstance, not only different loading conditions, which can be uneven within one single component, but the component curvature itself influence the stress state in TBCs [27,28]. Furthermore, the glazing approach on its own alters the stress state of the system by

the addition of a stiff layer, which brings up the question of choosing the right glazing thickness. All these aspects need to be considered to enable a conscious design of the shielded-compliant coating.

To assess the influence of surface curvature and glazed layer thickness on the stress state of the coating as-is without grooving, this state can be calculated analytically, considering a simpler case – a surface with only one principal curvature (Fig. 3, a), that is, a surface curved in one plane. Each point of a curve on a cross-section can be approximated with its own cylinder (Fig. 3, b). A problem of thermally-induced stress in a coated pipe with a constant radius was previously addressed in various studies. Here, a solution presented by Guo et al. [29] is adopted and generalised for an arbitrary number of layers (see Appendix).

3.1.2. Influence of the grooving geometry

The solution to this thermally-induced stress problem can be utilised for a circular multi-layered geometry. However, to account for the presence of grooves or non-elastic material properties, any analytical solutions become a very challenging task (that is not the scope of the present study). In such a case, an FEA package (COMSOL) was employed. To increase computational efficiency in FEA, 2D geometry
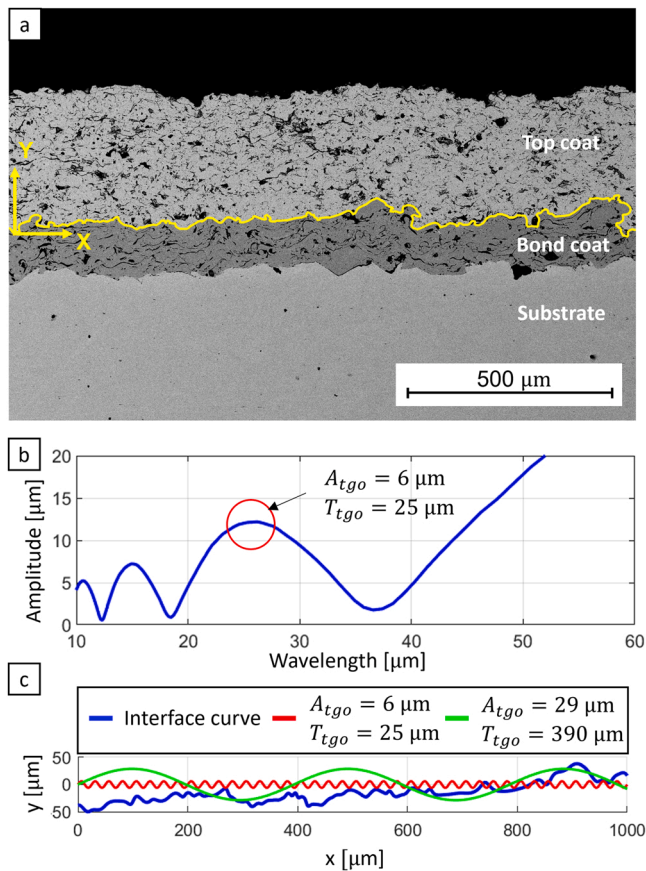
Fig. 5. Top coat – bond coat interface. (a) BSE image of as-sprayed coating showing irregular interface. (b) Amplitude – Wavelength chart obtained through FFT for the interface curve. The circled peak with a wavelength of 25 μm was chosen. (c) Interface curve and its sinusoidal constituents with 25 μm and 390 μm wavelengths.

was used with a generalised plane strain assumption. The coating system is represented by a multi-layered cylinder section with a variable radius R (Fig. 4, a). Microfeatures are controlled by 4 parameters: shape angle α, opening width b_2, depth h, and spacing S between adjacent grooves. To model an open geometry – the left edge A boundary condition was set to the symmetry and the right edge B to the symmetry with a free displacement, i.e. the edge is free to move but it must remain straight (Fig. 4, b). The thicknesses of all the layers were as follows: H_{sub} = 3.3 mm, H_{bc} = 0.1 mm, H_{tgo} = 1 μm, H_{tc} = 0.2 mm, H_{gl} = 0.1 mm.

The roughness of the BC-TC interface was approximated by a sine plotted along an arc, governed by the following equation:

$$\begin{cases} x(\varphi) = \left(R_{\text{int}} + A_{tgo} \cdot \cos(k \cdot \varphi)\right) \cdot \cos(\varphi) \\ y(\varphi) = \left(R_{\text{int}} + A_{tgo} \cdot \sin(k \cdot \varphi)\right) \cdot \sin(\varphi), \end{cases} \tag{1}$$

$$k = 2\pi / \left(T_{tgo} \cdot R_{int}\right), \tag{2}$$

where R_{int} – interface centreline radius [m], A_{tgo} – undulation amplitude [m], T_{tgo} – undulation period [m].

A fast Fourier transform (FFT) can be used to evaluate the most prominent harmonics in a rough BC-TC interface to model asperities [30]. Here, FFT was performed over the curve of the coating interface from the SEM image (Fig. 5, a) which showed the presence of several sinusoidal components (Fig. 5, b). A curve with A_{tgo} = 6 μm at T_{tgo} = 25 μm was chosen, curves below this wavelength show insignificant amplitude, and above – an excessive period, which implies more for the waviness rather than roughness (Fig. 5, c).

Thermo-mechanical properties of the TBC system used in the simulation are taken from the literature (Table A.1). Due to the large thickness of the substrate and weak plastic properties of the ceramic - the substrate, TC, and the glazed layer are assumed to behave elastically. In the case of TGO and BC, the behaviour was set to entirely plastic (Table A.2). The reference i.e., stress-free temperature for the system is set to 20 °C.

All materials, except for the substrate, were subjected to creep relaxation at high temperatures with power-law creep:

$$\dot{\varepsilon}_{creep} = A \cdot \sigma^n \ [\text{s}^{-1}] \tag{3}$$

Provided that the glazed layer and the top coat are the same material, their creep properties were assumed to be the same (Table A.3). However, this can only be used as an approximation due to the different microstructures of the layers.

To simulate the behaviour of the system at a high temperature, the external loads were set to isothermal heating from 20 °C up to 1050 °C for 5 cycles, consisting of heating (100 s), dwelling (7200 s), and cooling (100 s) stages (Fig. 4, c-d).

3.1.3. Influence of the shielded compliance modification on coating's buckling

Coatings can experience a variety of failure types, and buckling, being typical for EB-PVD, is not common for APS coatings. However, if to consider that pillars in the top coat crack and the fractured area is large enough, buckling can happen. Firstly, there is a dense rigid glazing layer that will build up large compressive stresses upon cooling due to creep. Secondly, the out-of-plane (Y-direction) stiffness of the top coat – glazing system is greatly reduced by introducing grooves. These factors can be considered in the buckling analysis of the system, eliminating the risk of detrimental premature failure.

Estimation of the critical stresses for a clamped compressed film can be given as [31]:

$$\sigma_c = \frac{\pi}{12} \cdot \frac{E}{1 - \nu^2} \cdot \left(\frac{t}{b}\right)^2 \ [\text{Pa}], \tag{4}$$

where E – Young's modulus [Pa], ν – Poisson's ratio, t – film thickness [m], b – delamination half-width [m].

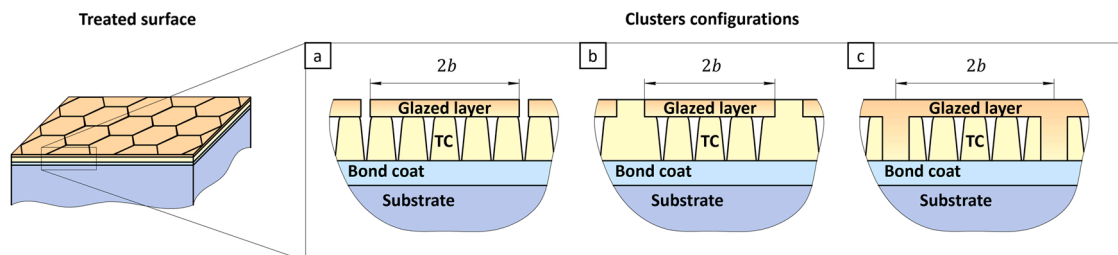If to solve it for b, a critical value of delamination (film size) can be

Fig. 6. Antibuckling clusters design of shielded-compliant coating. The width of each patch is defined as $2b$. (a) Patches are formed by cut-outs in the glazed layer. (b) Patches are formed by partial glazing with an untouched top coat around them. (c) Patches are formed by a deeper remelting during glazing. Dense zirconia boundaries clamp the rigid film.

Table 1

TBC material composition in used samples (as-sprayed condition).

Layer	Top coat	Bond coat	Substrate
Material	8%-YSZ	NiCoCrAlY	Nimonic C263
Thickness [mm]	0.3	0.1	3.3

calculated:

$$2b = \sqrt{\frac{\pi}{3} \cdot \frac{E}{1-\nu^2} \cdot \frac{t^2}{\sigma_c}} \; [\text{m}]. \tag{5}$$

It can be seen from Eq. (5) that the film stability can be improved by increasing the film thickness, given that Young's modulus and compressive stresses are characteristics of the material and operational conditions. However, in the case of the glazed layer, it may not be the best option, because of its rigidity due to a dense microstructure. A more feasible approach would be using this formula to separate the glazed layer into clusters with dimensions below the critical value of $2b$. Buckling elimination by segmentation was successfully demonstrated by Smialek [13] for plasma-sprayed coatings. This paper proposes several clustered arrangements of the shielded-compliant coating: by grooving the glazed layer (Fig. 6, a), by incomplete surface remelting (Fig. 6, b), or by a complete remelting of the top coat in a grid-like manner (Fig. 6, c). All of them would increase the stiffness of the glazing layer in the out-of-plane direction, however, the first option (a) is easier to implement compared to partial glazing (b) and it does not cause a risk of dense pillar cracking due to rigidity as for complete remelting (c).

Even though Eq. (5) describes the nature of buckling, it does not consider the stiffness of the top coat affected by the presence of the grooves, and the fact that there is not just a single material, but a top coat-glazed layer composite. Therefore, a linearised buckling analysis was carried out in COMSOL. The TBC system was cooled down to the reference temperature with the assumption that there is a crack in the top coat layer. The length of the crack was varied to determine the cluster size.

3.2. DIC for in-situ SEM heating experiment

To assess the performance of the shielded-compliant structure (i.e. grooves and glazing) and its fundamental purpose – to make the coating more compliant, releasing thermally-induced stresses – it is needed to measure either stresses or strains due to heating. This study utilises DIC to calculate displacements (and subsequent deformations) of small pixel groups between two images, one of which corresponds to a reference (stress-free) state, and another – to a loaded state. The resulting strain map can be converted to a stress map directly by extracting mechanically induced strains.

For the DIC experiment, small TBC coupons (8 x 25 x 3.7 mm, Table 1) were consequently machined with three laser systems (Fig. 7, a I-III). To eliminate the influence of one grooving pattern on others within one sample, two deep grooves (0.3 x 0.64 mm) along the Z direction were produced with a nanosecond laser (SPI SP-20 P-SM, 1064 nm) (Fig. 7, a-I, b), going through all three TBC layers. The maximum fluence was 130 J cm^{-2} at a 16 kHz frequency with a spot size of 35 μm and pulse width of 250 ns. The beam was scanning the
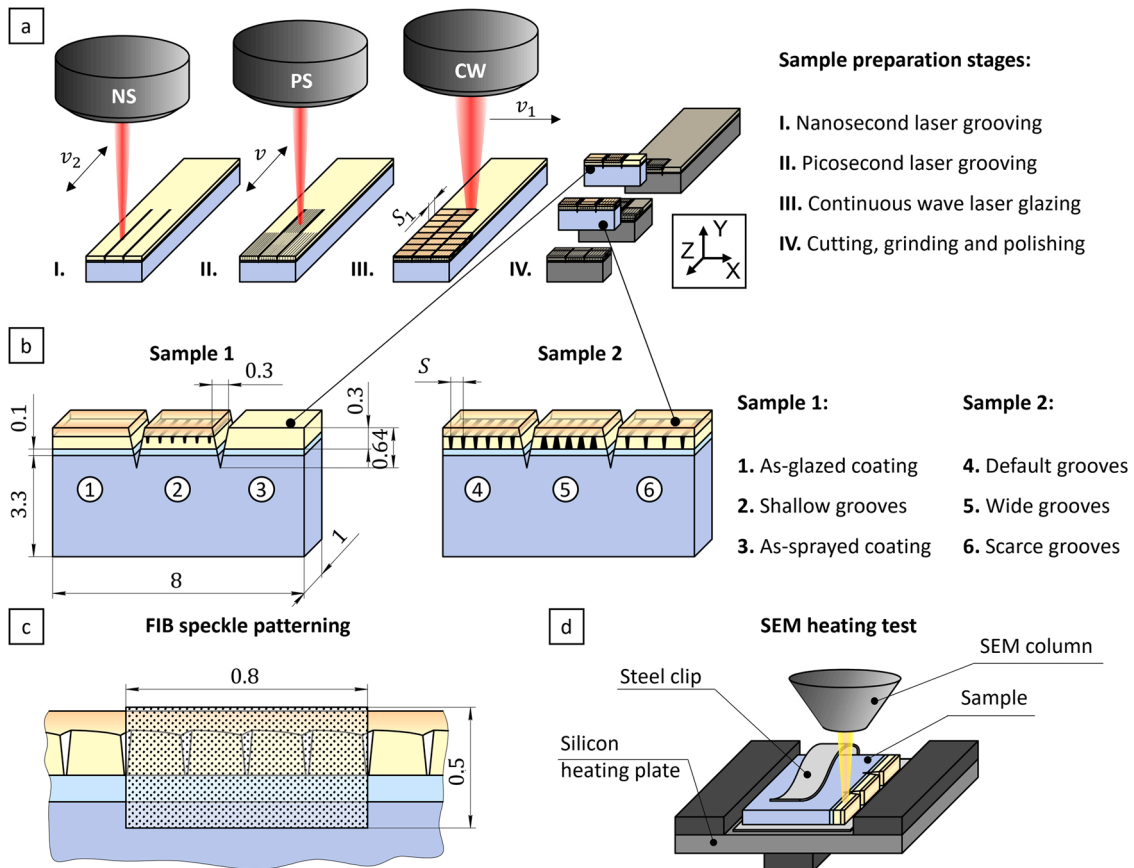
Fig. 7. DIC sample preparation and geometry, dimensions are given in mm. (a) Sample preparation stages – laser grooving, remelting, and cutting. (b) Thin sample geometry. Samples are represented by plates of TBC 1 mm thick, where the part is separated into 3 regions by nanosecond grooves to minimise their influence on each other. Each region has a specific picosecond grooving arrangement. (c) Area for FIB speckle machining. (d) Heating experiment arrangement. The sample is mounted on the heating plate and is held by a steel clip, which is attached with a high-temperature carbon glue to the plate. During heating, the sample surface is scanned with an SEM electron beam.

Table 2
Laser processing parameters.

	Picosecond grooving stage			
	Shallow	Default	Scarce	Wide
Fluence [J cm^{-2}]	66	66	66	55
Frequency [kHz]	4	4	4	4
Scanning speed v [mm s^{-1}]	35	35	35	60
Laser spot size [μm]			35	
Pulse width [ps]			60	
Repetitions N	120	220	220	200
Spacing S [mm]	0.2	0.2	0.3	0.2
$\varphi_{L/R}$ [°]	-	-	-	-15/+15
Angular divisions N_a	-	-	-	7
	Glazing stage			
Power [W]			100	
Scanning speed v_1 [mm s^{-1}]			50	
Laser spot size [μm]			400	
Spacing S_1 [mm]			0.32	

0.25 mm wide trench with a 0.025 mm step size for 2000 repetitions at 400 mm s^{-1}. To increase the material removal efficiency, every 50 repetitions the beam was refocused on 50 μm.

In the second stage, four different patterns were grooved in the Z direction with a picosecond laser (EKSPLA AtlanticHE, 1064 nm) (Fig. 7, a-II). Then, the outer TC surface was remelted with a continuous laser (SPI SP100C, 1090 nm) in the X direction, bridging the grooves with a glazed layer (Fig. 7, a-III). One of the areas on the sample was masked during glazing to retain an as-sprayed coating.

The Murano 525 heating stage was used to heat the samples to the temperature of 600 °C during the in-situ experiment on JEOL 7100 F field emission gun scanning electron microscope (FEG-SEM). This top limit was set to minimise the risk of damaging the electron column, as the observed area was large, and no shielding was used. Although this is not an operational temperature of the coating, it enables the validation of the model and, thus, performing the shielded compliance modification in a scientifically conscious manner. Given that the maximum sample size for the stage is 4.5 x 9 x 3 mm, after laser machining samples were cut and mounted in KM-BACK resin for consequent grinding and polishing until the desired thickness of 1 mm was achieved (Fig. 7, a-IV). This resin was dissolved in acetone at 50 °C, and samples were cleaned with isopropanol. The small thickness of the sample is dictated by heating conditions, as minimising the thickness reduces the thermal gradient between the heated bottom and observed top surfaces.

Two samples were produced, containing a total of 6 different regions (Fig. 7, b) – as-sprayed and as-glazed coating, as well as various groove arrangements: shallow, default, scarce and wide (Table 2).

During the second stage of the modification many factors vary the melting/solidification conditions: surface light absorptivity, remelt flow velocity, cooling rates, and specimen geometry. Furthermore, the presence and the geometry of grooves change the surface tension effects and cooling conditions, affecting the flow and temperature distribution. In this regard, the problem of creating a glazed layer of particular morphology and microstructure is complex, involving consideration of all of the processing conditions. It can be solved by implementing an analytical or numerical (e.g. FE) model to account for all the effects or by optimising the laser parameters for a specific grooving arrangement through a set of experimental tests. In the present study, laser glazing parameters were derived from a series of tests, aiming at the production of a continuous layer bridging the gaps, and kept constant for all of the grooving arrangements.

DIC analysis requires the observed surface to be patterned with *speckles* to enable robust indexing of different subsets and their deformations. On the microscale, such a random dotted pattern can be created intentionally using the focused ion beam (FIB). However, unintentional morphological features (cracks, pores, cutting marks etc.) can also provide sufficient results [32,33]. But since the glazed layer has

no distinguishable features to index, a speckled pattern of 1 μm sized dots was produced on the samples (Fig. 7, c) covering the area of 0.8 x 0.5 mm using the focused ion beam (FEI Quanta200 3D FIB-SEM). The speckle was generated by a pseudorandom algorithm from Correlated Solutions, however, in combination with a unique microstructure of the TBC, the resulting image was presenting a completely random surface for stable DIC indexing. The surface was milled by gallium ions with a current of 3 nA at 30 kV for 1 h. Such parameters were selected to produce a visible pattern of submicron depth at the shortest exposure, thus reducing the damage from milling as much as possible.

To prevent constraining the face of the sample with the high-temperature carbon cement, which can disrupt the free thermal expansion, a fixturing clip was used. This clip was glued to the silicon heating platform with the carbon cement and the sample was placed inside (Fig. 7, d).

During the test, samples were gradually heated from 23 °C to 600 °C with a 100 °C increment and left to dwell for 30 min at each step to establish thermal equilibrium. Once the image at the maximum temperature was acquired, samples were cooled down and left for 1.5 h in SEM to ensure an even room temperature of 23 °C (taken as a reference for the analysis). An additional image was taken after cooling down, as the speckle pattern tended to deteriorate during exposure to the elevated temperature, therefore DIC algorithm could experience issues at indexing using a pre-heating image as a reference.

The present study utilises an open-source 2D DIC code based on MATLAB – Ncorr [34] – to calculate the total strain values developed by the sample. DIC processing parameters were chosen based on the sensitivity study (Fig. A1). For a larger size of each subset, its total determined displacement decreases; a larger strain radius, used in calculating the derivative from the displacement field, smoothens up all local strain bursts (Fig. A1, c). At the same time, higher analysis resolution presents noisy artefacts, created by misindexing and morphological features (pores). Nonetheless, the processing parameters hardly affect averaged values (Fig. A1, a and b) except for the interfacial regions. Considering this, for the DIC study the following parameters were selected: a subset radius of 18 pixels spaced 2 pixels apart, and the radius used for strain calculation of 15 subset points. Even though relaxed DIC parameters may blur local strain changes produced by natural microstructural irregularities or interfacial undulations, the focus of the study is on large-scale strain effects induced by the shielded-compliance modification.

However, for the analysis of the shielded-compliant structures, the 'measured' strain data is converted to stress. Because stresses are of great use from a practical perspective for determining the durability of the component or for assessing strain tolerance as a property of developing smaller stress. To do this, the total strain can be decomposed into the thermal and mechanical portions:

$$\varepsilon_{DIC} = \varepsilon_{mech} + \varepsilon_{therm}, \tag{6}$$

$$\varepsilon_{therm} = \alpha(T) \cdot (T - T_{ref}), \tag{7}$$

where $\alpha(T)$ – coefficient of thermal expansion [°C^{-1}], T – current temperature [°C], T_{ref} – reference (stress-free) temperature [°C].

If there are any mechanical loads or the degrees of freedom of an object are restrained, mechanical strain arises. In the case of TBCs, the mechanical portion additionally develops due to the mismatch of thermal expansion coefficients. This is the one associated with stresses, which can be calculated using the full combination of strain components by Hooke's law:
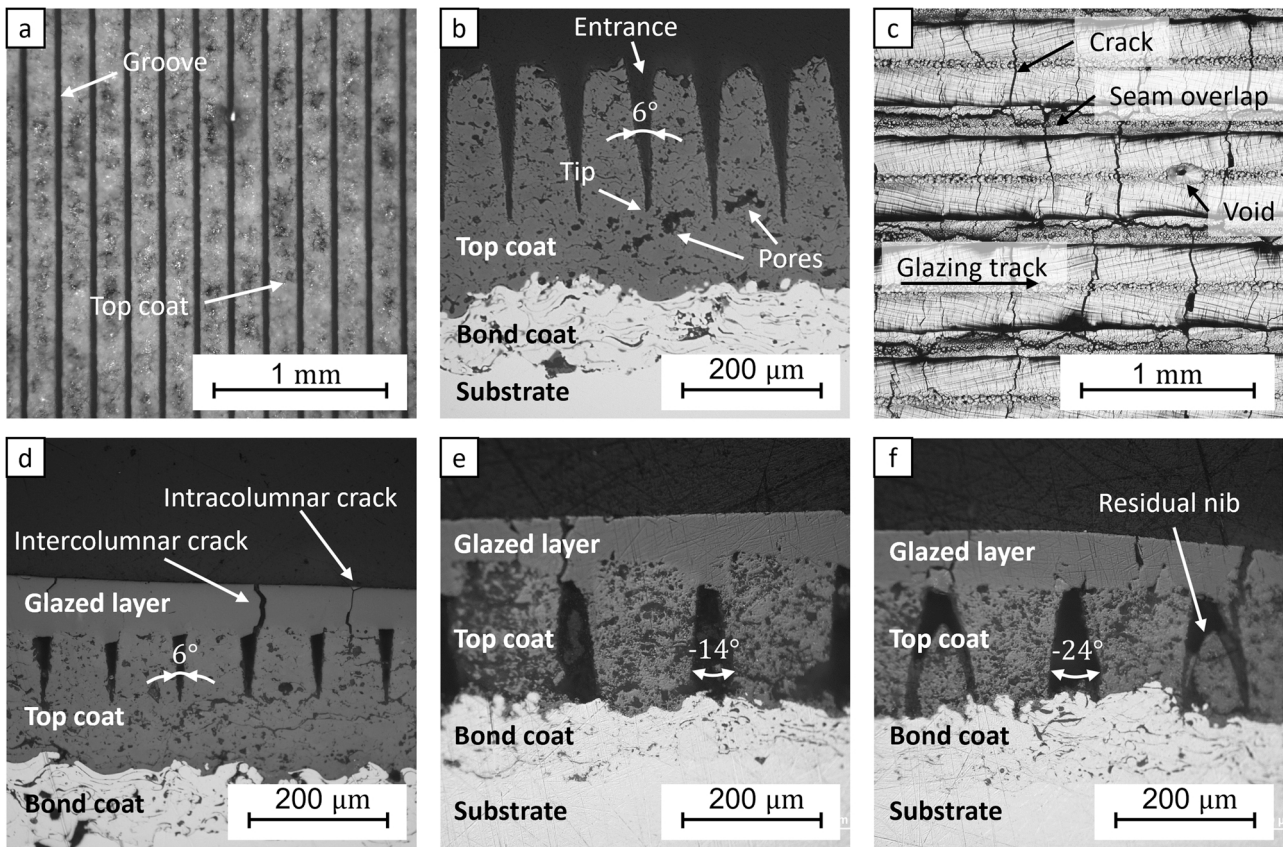
Fig. 8. Top coat after laser modification. (a) Top view of the grooved coating, no rotation: $S = 0.2$ mm, $N = 220$. (b) The cross-section of the grooved coating, no rotation: $S = 0.1$ mm, $N = 220$. (c),(d) Top view and the cross-section of the grooved and glazed coating, no rotation: $S = 0.1$ mm, $N = 120$. (e) Wide grooved and glazed coating: $S = 0.2$ mm, $N = 200$, $\varphi_{L/R} = \pm 10°$, $N_a = 5$. (f) Wide grooved and glazed coating: $S = 0.2$ mm, $N = 200$, $\varphi_{L/R} = \pm 15°$, $N_a = 7$.

$$\sigma_x = \frac{E}{(1+\nu)(1-2\nu)}\left((1-\nu)\varepsilon_x + \nu\left(\varepsilon_y + \varepsilon_z\right)\right) \text{ [Pa]};$$

$$\sigma_y = \frac{E}{(1+\nu)(1-2\nu)}\left((1-\nu)\varepsilon_y + \nu\left(\varepsilon_x + \varepsilon_z\right)\right) \text{ [Pa]}; \qquad (8)$$

$$\sigma_z = \frac{E}{(1+\nu)(1-2\nu)}\left((1-\nu)\varepsilon_z + \nu\left(\varepsilon_x + \varepsilon_y\right)\right) \text{ [Pa]};$$

$$\tau_{xy} = G \cdot \gamma_{xy} \text{ [Pa]};$$

$$\tau_{yz} = G \cdot \gamma_{yz} \text{ [Pa]};$$

$$\tau_{xz} = G \cdot \gamma_{xz} \text{ [Pa]}.$$

All 3 strain components (i.e. x, y, z) should be known to evaluate the stress state (or 6 if to include shear stresses). Since 2D DIC analysis provides only a planar strain state, an approximation of the problem is needed.

The plane stress assumption is not applicable due to the thick Z dimension of the coating relative to its XY dimensions. The plane strain assumption can be used only as a rough estimation because the XY faces of the sample are not restrained. A more reasonable 2D approximation is generalised plane strain, i.e. the Z strain component is independent of X and Y ones. This paper employs the assumption that the strain in the Z direction depends only on thermal expansion coefficient mismatch and does not depend on the XY grooving geometry of a sample, or in other words, the unknown Z strain component is determined from the biaxial stress state which is often used in TBC stress modelling. In the case of biaxial stress, the total elastic strain (thermal + mechanical) in any layer of the TBC system can be calculated [35]:

$$\varepsilon_z = \frac{E_{sub}t_{sub}\alpha_{sub} + E_{bc}t_{bc}\alpha_{bc} + E_{tgo}t_{tgo}\alpha_{tgo} + E_{tc}t_{tc}\alpha_{tc} + E_{gl}t_{gl}\alpha_{gl}}{E_{sub}t_{sub} + E_{bc}t_{bc} + E_{tgo}t_{tgo} + E_{tc}t_{tc} + E_{gl}t_{gl}} \cdot \left(T - T_{ref}\right). \qquad (9)$$

3.3. Material analysis

Since laser ablation is associated with considerable heat input to the material, the coating structure is expected to be affected after grooving. Nonetheless, glazing causes the YSZ recrystallisation and the creation of a significantly different microstructure. This brings the need to inspect the TBC after the modification process from a material point of view. Morphological features were observed on the Quanta 650 SEM and JEOL 7100 F FEG-SEM. However, to reveal the laser-induced changes to the grain structure, electron backscattered diffraction (EBSD) was utilised via the Nordlys Max 3 detector (Oxford Instruments). It allowed assessing the grain size and orientation in the glazed layer, as well as the residual plastic deformation of the coating, which was visualised through the low-angle local misorientation (0–5°) as it does not account for grain boundaries [36].

To check whether the chemical composition of the YSZ experienced any redistribution of the elements, the electron diffraction spectroscopy (EDS) analysis was employed while the EBSD data was collected via the X-max 150 detector (Oxford Instruments).

Preparation of the cross-section surfaces for the microscopy was guided by standard metallographic procedures: cold mounting, grinding and polishing. However, before SEM imaging the samples were coated with an 8–15 nm layer of carbon at EDWARDS E306 and Quorum Q150R ES coaters.
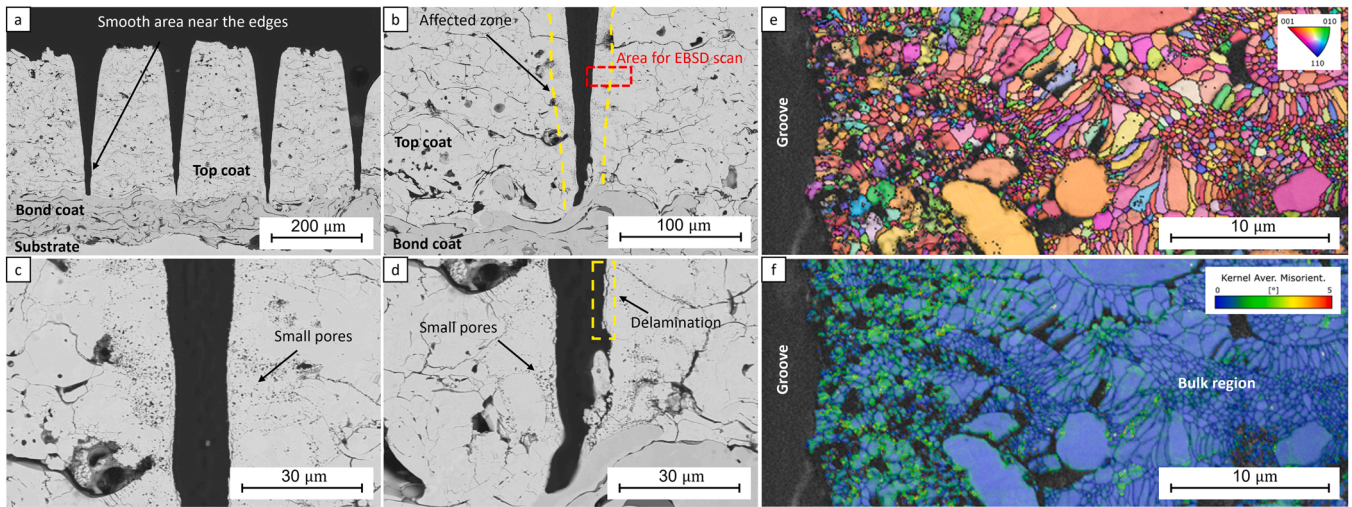
Fig. 9. Cross-section SEM images of laser-induced damaged areas in a grooved sample. (a) – (d) SEM images showing a modified area around the groove's edge. (e), (f) EBSD and kernel average misorientation maps of the laser-damaged edge.

4. Results and discussion

4.1. Study of the macro- and microstructure of the shielded-compliant coating

At the first stage of the modification, the coating is irradiated with a picosecond pulsed laser, which is scanned along the grooving direction N times (Fig. 2, b-1), to produce grooves (Fig. 8, a, b). They would allow for increasing the TBC thermal compliance by reducing the thermal mismatch between the layers. After grooving, the coating's surface does not show any signs of induced damage. The grooves are straight, with little variance in the width (30 – 40 μm), and there are no visible cracks or remelted material on the top surface. This is mainly due to the short thermal diffusion length during short pulse ablation: the material absorbs laser energy in a limited volume, which leads to higher processing accuracy and stability.

Due to the laser defocusing with the increase of ablation depth, a straight groove has a V-shape cross-section (Fig. 8, b, d) with $\alpha = 6°$ angle, i.e., a positively tapered groove ($b_1 < b_2, \alpha > 0$). To achieve a negatively tapered (dove-tail) groove where $b_1 > b_2$ ($\alpha < 0$) (Fig. 8, e, f), additional angular divisions need to be applied during laser machining (Fig. 2, b). Such grooves are expected to have better compliance to thermally-induced stress and a longer cycling life, due to decreased thermal mismatch between the top and the bond coats. Even though not all the material is removed from the dove-tail grooves, leaving a nib in the middle, this residual is disconnected from the glazed layer and will not participate in the coating's operation.

Interestingly, the machining conditions used for negatively tapered grooves utilise a higher scanning speed than for positively tapered ones (Table 2, default), but at the same time, the trenches around the nib reach the bond coat as well. Since the strategy for ablating wide grooves begins with creating the middle trench (Fig. 2, b-1), its depth is represented by the tip of the nib (Fig. 8, f). As soon as the gap opening (b_2) gets bigger, at latter passes with rotations of the specimen, the laser beam is guided though the middle trench and can initiate ablation already inside of the top coat. This fact suggests that negatively tapered grooves can be machined using parameters for grooves of half TC layer deep ($h = 0.5H_{tc}$), increasing the overall machining efficiency and reducing the thermal damage, compared to the full-depth ones.

A typical glazed surface is obtained by overlaying single-pass tracks (Fig. 8, c). The cracks appear perpendicular to the glazing direction, and most of the time are aligned with the grooves (Fig. 8, d-f). This happens when the material starts to solidify and contract. The adhesion to the as-sprayed coating allows the remelt to stick to it, and the separation

initiates in the grooved section. However, in some cases, if the bridge over the gap is already formed and solidified, the cracking can be induced in the as-sprayed area, fracturing the pillar. Even though the crack in the glazed layer is a potential gate for the hot gas and CMAS infiltration, it promotes the compliance of the whole structure, reducing thermally-induced stresses in the coating.

Although the main scope of the study is geometry and arrangement influence of micro features on the performance of the coating, their production is associated with a highly energetic process, thus laser-induced damage is of great concern. A grooved sample (Table 2, default grooves) shows a reduction in cracks (originating from the splat-like structure) in the affected zone near the groove edges, making them look *smooth* (Fig. 9, a-d). This crack closure can be associated with a sintering effect due to the heat during machining, which leads to a more dense and brittle material. A distinct near-edge zone is present, where the material contains small micropores. The recast material is not noticeable, however, there is some minor spallation at the edges. Noteworthy, that picosecond energy fluence was above the ablation threshold for the top coat and below the one for the bond coat. This allowed making the grooving process more controllable, as when the trench approaches the bond coat the light is scattered and reflected at the interface, which causes the groove's tip to dogleg and widen (Fig. 9, d). This fact is of particular convenience because even with the BC-TC interface being wavy the groove will reach the bond coat and will not remove it.

The EBSD of a groove's edge with a 70 nm step size was carried out (Fig. 9, e) to assess the crystalline structure of the modified region, showing the edge to consist mainly of small grains with embedded pores. Those pores could be a result of thermally induced chemical reactions, however, EDS analysis did not show any uneven chemical element distribution. In such a case, this may signify an irreversible deformation. Similar grain fragmentation can be observed after mechanical machining due to strain localisation [37].

Generally, it is assumed that picosecond scale machining does not bring any significant thermal damage due to shorter diffusion length when compared to other long-pulsed (e.g., nano- or microsecond) or continuous lasers [38]. This length for sub-nanosecond pulses is almost independent of the pulse width [39]:

$$l \approx a\sqrt{\frac{M_{ion}}{3m_e}} \text{ [μm]}, \tag{10}$$

where a – average interatomic distance [μm], M_{ion} – mass of an ion [amu], m_e – mass of an electron [amu].
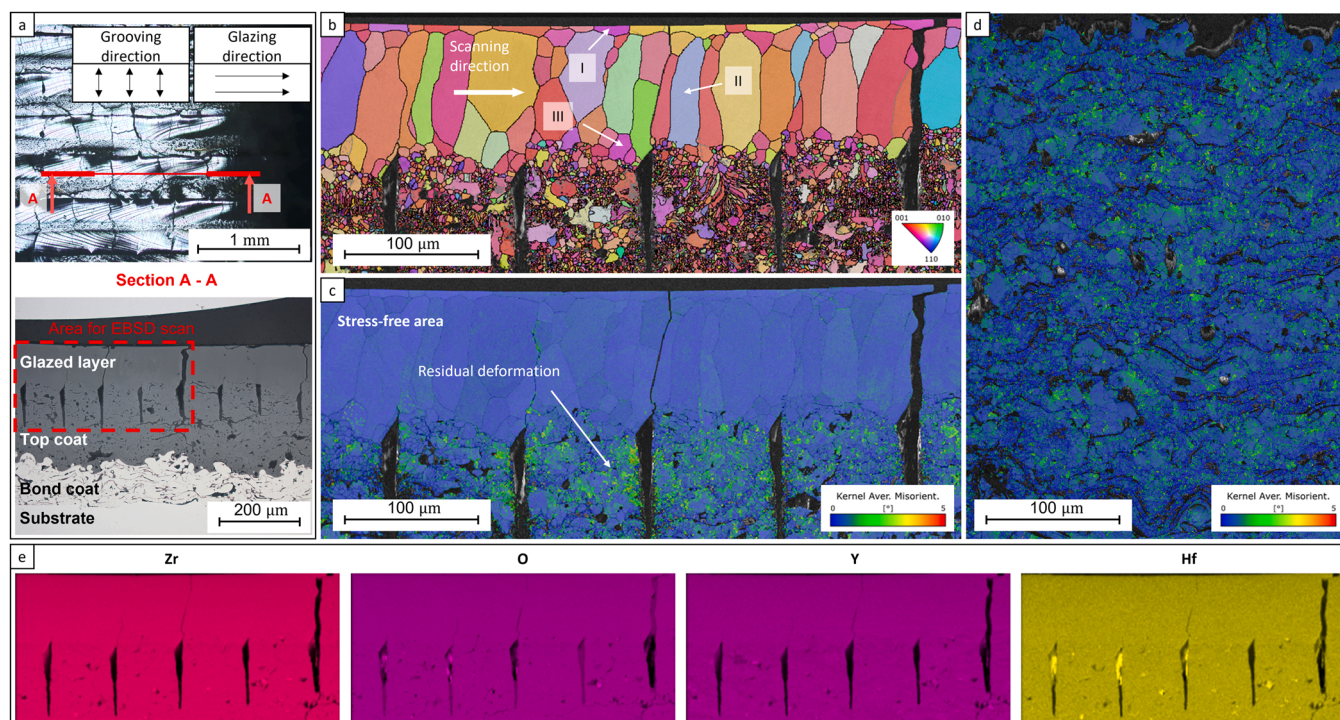
Fig. 10. Microstructural characterisation of the top coat. (a) Top and cross-sectional view of the grooved and glazed sample. The area for the EBSD map is outlined in red. (b)-(c) IPF and kernel average misorientation maps of the grooved and glazed coating. (d) Kernel average misorientation maps of the initial as-sprayed coating. (e) EDS distribution of the chemical elements in the sample after processing.

As a rough estimation, the body-centred cubic (BCC) zirconium can be used [40]:

$$M_{ion}\left(Zr^{4+}\right) = 91.22 \text{ amu},$$

$$m_e = 0.00055 \text{ amu},$$

$$(11)$$

$$a = 3.14(17)\cdot10^{-5}\cdot T + 3.579(5) = 3.589 \text{ Å } (T = 293.15 \text{ K}).$$

Under these conditions, $l = 0.15$ µm, however, the kernel average misorientation map shows a distinct difference between the bulk and the edge areas at a larger scale (Fig. 9, f), indicating residual deformation on a sub-granular level. From this map, the damaged zone thickness can be estimated to be about 10 µm, which is two orders larger than that obtained from Eq. (11). A noticeable misorientation in combination with pores and the absence of any chemical reactions in the damaged zone may suggest that the refinement was induced by plasma shock waves which can be of a GPa magnitude [41]. Fractured grains and pores can become nucleation sites for thermal fatigue cracks leading toward the reduction of the lifetime of the coating [42]. Pulses with lower energy or the application of inert assist gases (to replace oxygen from the air) can decrease the plasma pressure and minimise the damage to the coating; however, this is out of the scope of this paper.

As it was stated above, laser glazing can enhance the performance of the TBC, by modifying its metallurgy. To reveal the metallurgical changes and to make insights into possible glazing benefits, its microstructure was analysed. The grooved and glazed sample (Table 2, shallow grooves) was cross-sectioned along the glazing track, however from an SEM image, it is difficult to judge changes in the remelted layer, aside from visible densification (Fig. 10, a). Therefore, an indicated area of section A-A was used for EBSD analysis with a 530 nm step size.

The glazed layer has a constant depth of approximately 100 µm, with only a slight variation because thermal equilibrium during remelting is interrupted by grooves (Fig. 10, b). This layer visually can be separated into three zones: *I* - the zone of thin lateral grains, which grow along the outer surface from periphery to the centreline of the melt pool; *II* - the

zone of long columnar grains, growing along the thickness of the layer; *III* - the zone of smaller equiaxed grains, located mainly near the as-sprayed region. The columnar grains form the main part of the glazed layer, and thus, are expected to be responsible for the enhanced properties. The reduced number of grain boundaries and absence of pores providing better oxidation and corrosion protection, also suggest an increased hardness and toughness of the structure, which will be reflected in higher resistance to abrasive erosion. The effective cohesion of the layer is increased due to the smaller number of grain boundaries, which hinders crack propagation, as more energy is required to create new free surfaces. However, if the crack path aligns with the grain boundary – the spallation may occur easier than for a fine-grain structure, as almost no branching is required for the crack to propagate through [43]. At the same time, straight columnar grains can act as a PVD system, where on heating they can expand into the intergranular space around them, releasing thermally-induced stress and promoting a longer cycling life of the TBC.

From the KAM map (Fig. 10, c) another distinctive feature is observed – the glazed layer has almost negligible intergranular misorientation as expected to be in pristine and non-strained crystals. And even though KAM does not automatically indicates stress but geometrically necessary dislocations, the glazed layer can be considered as almost *stress-free*, compared to the grooved region, which is the initial coating. It can be argued that deformations in the grooved regions were induced by grooving itself or by the contraction of the glazed layer during its solidification. To understand this, the KAM map of the as-sprayed intact coating was made (Fig. 10, d), which indicates a presence of a comparable amount of residual plastic deformation throughout the coating bulk. In this regard, it is suggested that this strain was induced in the TBC by the spraying process, and then it was relieved by relatively slow and uniform recrystallisation during the glazing stage. As it is widely known, after deposition APS TBCs can develop residual tensile stresses, thus the absence of pre-stress conditions can also be seen to increase TBC durability. Moreover, the conducted EDS analysis did not reveal any chemical elemental redistribution after glazing (Fig. 10,
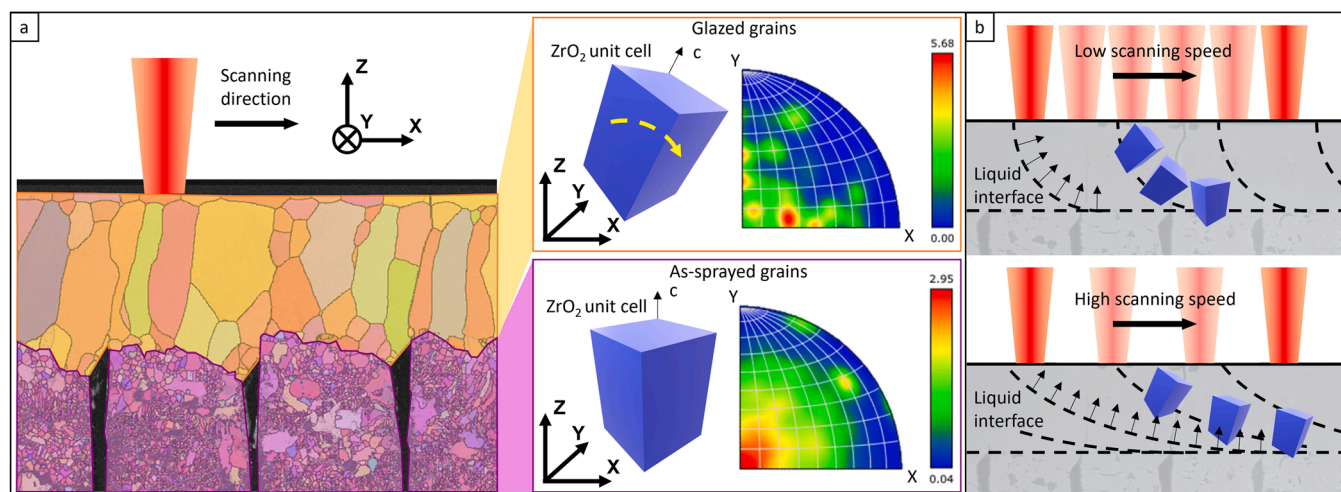
Fig. 11. Zirconia unit cell orientation after remelting. (a) Pole figures of glazed and as-sprayed regions of the coating. The zirconia unit cell tilts towards the scanning direction (X) of the laser. (b) Comparison of the liquid interface during remelting with low and high laser speeds. The grain unit cell orients along thermal gradients.

e). It means that there is no yttria depletion which could cause instabilities in the phase composition.

Interestingly, the crystallographic orientation of the grains is also altered when remelting. The initial as-sprayed region consists of mainly vertically oriented grains, where the c-axis of a tetragonal unit cell is oriented along spraying direction Z (Fig. 11, a). But after glazing new peaks in the pole figure are observed, where the cells are tilted towards the scanning direction (X). The fact that there is a change in crystallographic orientations dependent on scanning direction, brings a promising possibility to controlling these orientations. For instance, Zhang et al. [44] showed that the fracture toughness of 3 mol% yttria-stabilised tetragonal zirconia along the [001] direction is almost 50% higher than for the non-textured isotropic coating. Given that the single crystal YSZ shows anisotropy, and the size of glazed grains makes them locally anisotropic on a macro scale, a further investigation may enable the possibility to tailor the glazed layer microstructure according to the operational conditions. For example, by changing the laser scanning speed and consequently the melt pool shape, the orientation of the grains can be altered (Fig. 11, b). This can be done, to align the [001] direction of grains with the anticipated direction of foreign objects or abrasive particles colliding into the coating. Specific laser parameters providing an optimal microstructure may be obtained during the experiments or by using modelling approaches, as was shown by Ushmaev et al. [45].

To conclude, although, selected laser parameters were based on the criteria of minimal damage grooving and the glazed layer continuity, the presented morphological features clearly indicate an improvement of the thermal cycling life, as well as the environmental protection (erosion, oxidation and corrosion), due to the following factors:

- Strain-tolerant grooves with the absence of detrimental cracking;
- Continuous dense remelted layer with insignificant porosity and less grain boundary density;
- Almost a stress-free state of the remelted layer due to recrystallisation;
- Large columnar grains, further promoting strain tolerance.

4.2. The effect of the component curvature and glazed layer thickness on the stress state of the TBC

Considering the relation of the laser processing parameters, dimensions of the grooves, and the results from the metallurgical study presented above, it is appropriate to assume, that similar macro- and microstructure will be obtained on surfaces close to real engineering

applications (e.g. non-flat). Therefore, there is an open question, how the shielded-compliant features will be designed for surfaces with varying geometry. An answer to this can be given by the stress analysis when varying not only the geometry of the features but the surfaces where they are generated. Although an analytical model [29] (see Appendix) cannot consider grooving influence, it can help to understand how the TBC system curvature and layer thicknesses affect the stress state.

Coating failure mostly occurs after cooling down to room temperature. However, from a practical perspective, initially, stresses appear due to heating to operational temperature, where the creep takes place. And then the creep will lead to stress development after cooling down. Therefore, high-temperature stresses can give an estimation of the coating's failure. Here, the analytical model was used to calculate the TBC systems with various surface radii and glazing thickness at a constant temperature of 1050 °C. And since for an accurate lifetime prediction, the model needs to incorporate many operational factors – creep, plasticity, sintering, oxidation and cracking – the analysis presented in the paper aims to provide a generalised understanding of shielded compliance effects on the durability of the TBC. In this regard, the stresses are plotted across the thickness of the TBC layers for each of the configurations.

Surface radius has almost no effect on the resultant in-plane (hoop) stresses (Fig. 12, a), however, as soon as the surface is curved the out-of-plane (radial) stresses arise in all the layers (Fig. 12, b). Given the temperature of 20 °C as a reference, the radial stress is compressive, because of the difference in CTE, where a highly expanded substrate is constrained by a less expanded top coat. In general, compressive stress is less likely to cause damage to the material, but if creep relaxation takes place in the system at a high temperature, then this stress can be reverted to tensile upon cooling. In this case, it may lead to the creation of cracks parallel to the interfaces of the layers, with a higher chance of spallation for a more curved surface. The same reasoning applies to the hoop stress, where the creeping coating develops compressive stresses on cooling and can potentially buckle.

Remelting of the as-sprayed system presents another layer, which strongly affects the stress distribution. Because this glazed layer has a relatively high Young's modulus and the same CTE as the TC, it creates even higher resistance against the substrate expansion than the TC alone. This fact explains the increase in compressive stresses across the layers (Fig. 12, c, d). Although presenting the tensile hoop stresses (Fig. 12, c), the glazed layer can develop massive compressive stresses (down to −1.8 GPa) after cooling down due to creep relaxation. And as for the as-sprayed system, the radial stress will revert to tensile (Fig. 12,
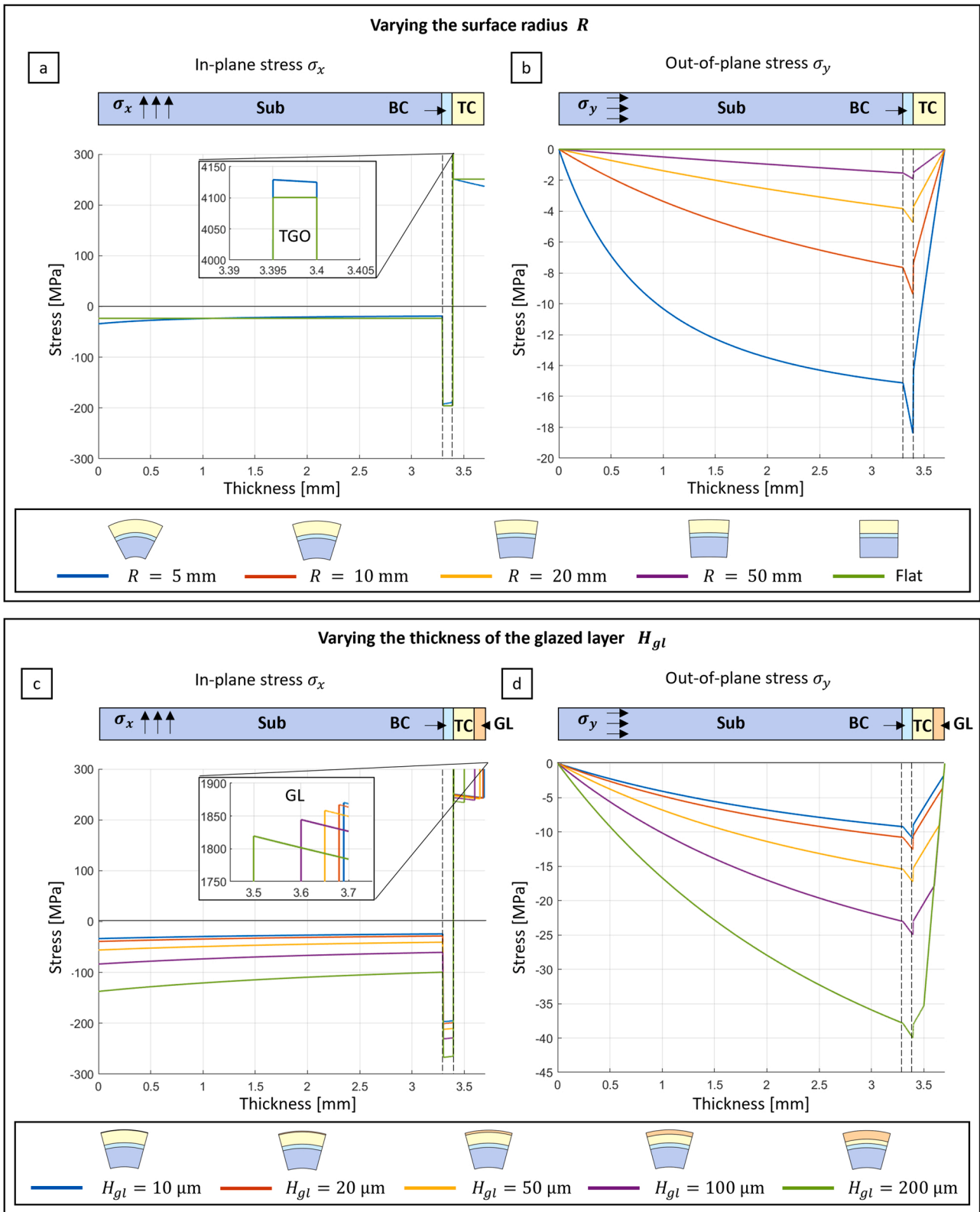
Fig. 12. Stress distribution through the thickness of the TBC at constant temperature $T = 1050\ °C$ from the analytic solution. Sub – substrate, BC – bond coat, TGO – thermally grown oxide, TC – top coat, GL – glazed layer. **Varying the surface radius R:** (a) As-sprayed coating, in-plane (hoop) stress, intermediate radii are not shown. (b) As-sprayed coating, out-of-plane (radial) stress. **Varying the thickness of the glazed layer H_{gl}:** (c) Glazed coating with $R = 10$ mm, in-plane (hoop) stress, TGO layer is not shown. (d) Glazed coating with $R = 10$ mm, out-of-plane (radial) stress.

**Varying the groove depth h **
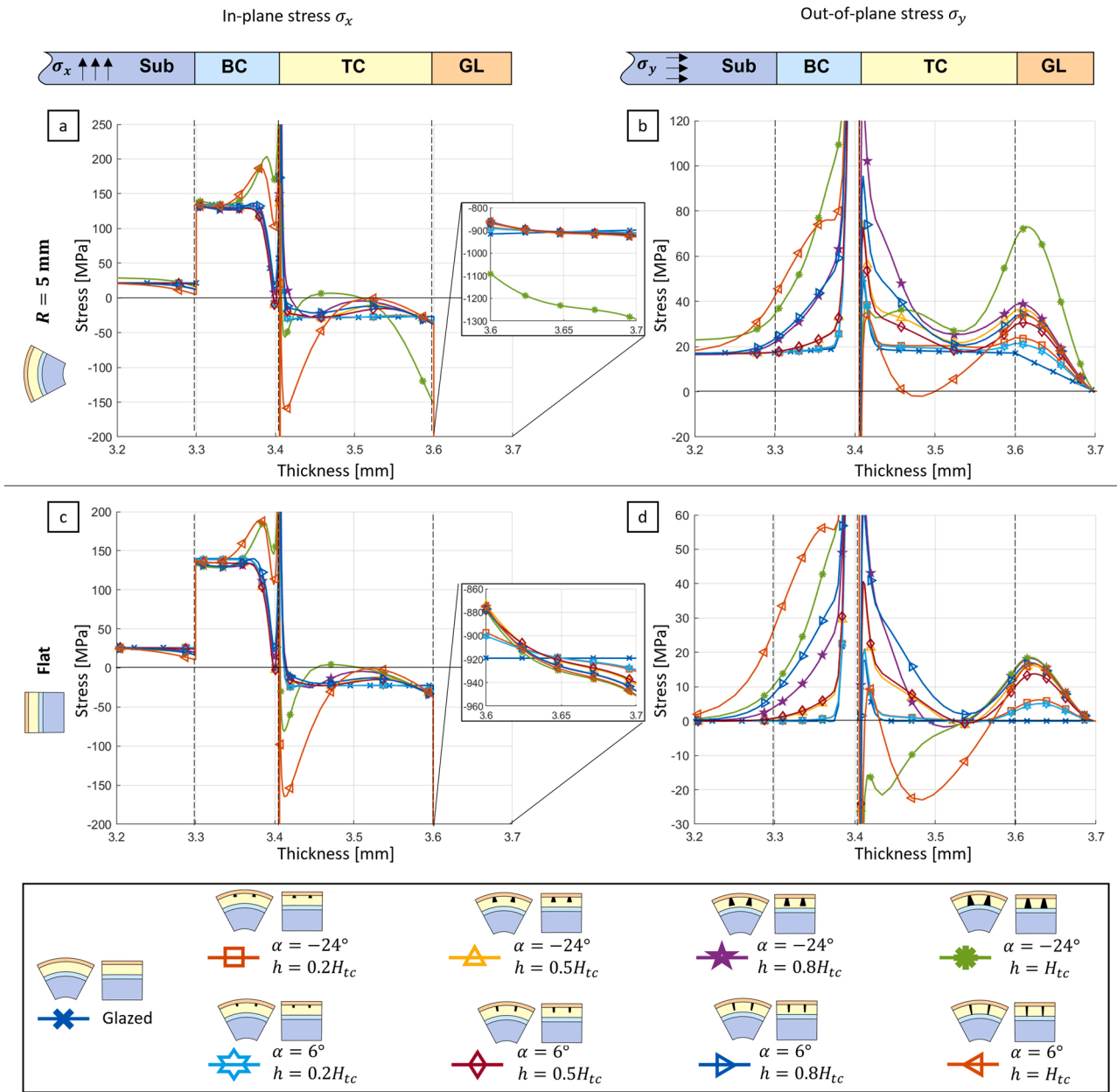
Fig. 13. The influence of **the groove depth h ** on the residual stresses in the section through the middle of the pillar after 5 isothermal cycles. Markers are plotted with a 5-data points spacing. (a), (b) Surface with radius $R = 5$ mm and (c), (d) flat surface; shape angle $\alpha = -24°$, 6°, spacing $S = 0.2$ mm, groove depth $h = (0.2–1)$ H_{tc} . Sub – substrate, BC – bond coat, TC – top coat, GL – glazed layer. (a), (c) In-plane (hoop) stress distribution. (b), (d) Out-of-plane (radial) stress distribution.

d), producing lateral cracking. This in combination with the compressive hoop stress suggests that the glazed layer is extremely prone to buckling. Under the same considerations, after cooling the substrate and BC will develop dangerous tensile stresses instead. As seen from the figure, one way to tackle it is by reducing the depth of the remelted layer. However, it may not be always feasible given the requirement for bridging the grooves. In such a case, buckling of the glazed layer can be eliminated by making it porous or separating it into smaller chunks to increase the out-of-plane stiffness.

4.3. The effect of the grooving geometry on the stress state of the shielded-compliant TBC

The influence of grooves on the system was assessed from FEA through residual stresses in the TBC after five isothermal cycles. They

were evaluated along edge A (Fig. 4), which represents a cross-section in the middle of the pillar, distanced from the grooves, so as not to account for the geometrical effects of stress concentration. The as-sprayed state is not shown because its residual stresses are very close to a just-glazed geometry with $H_{gl} = 100$ μm which was chosen as a baseline for the analysis. Firstly, the groove depth was varied (Fig. 13). As the stress relief effect is occurring in the in-plane direction (along the BC-TC interface), this direction may be used to assess the effectiveness of grooving. Given this, it can be concluded that grooves $0.2H_{tc}$ deep do not give any significant improvement, with only $0.5H_{tc}$ showing some noticeable stress reduction (Fig. 13, a, c). Once the groove approaches the whole TC thickness, the in-plane stress is majorly decreased, however additional stresses on BC and glazed layer interfaces arise, which may weaken the adhesion. The bond coat is almost unaffected by the in-plane stresses until the groove has a full thickness depth, which can be a
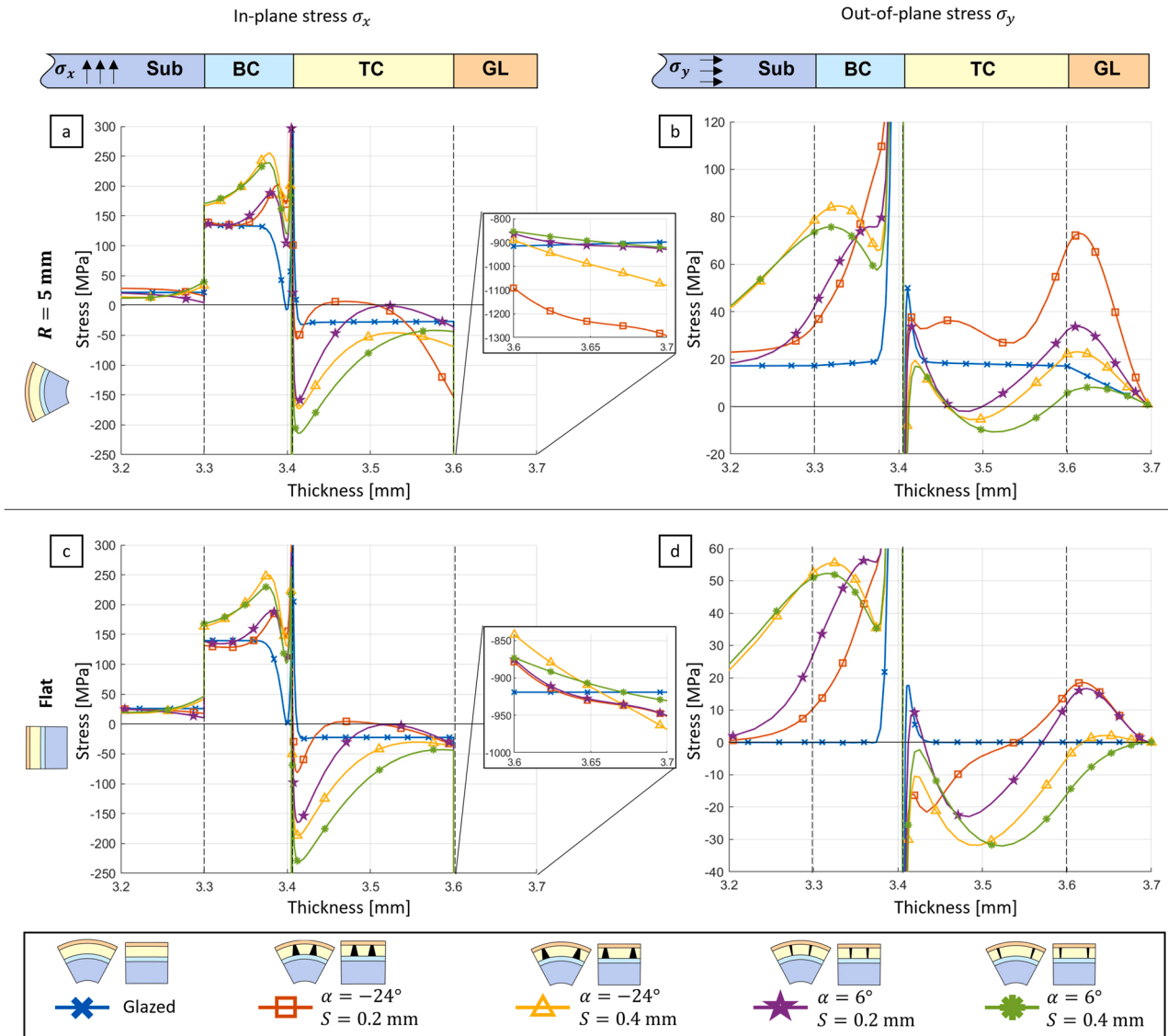
Fig. 14. The influence of **the groove spacing S** on residual stresses in the section through the middle of the pillar after 5 isothermal cycles. Markers are plotted with a 5-data points spacing. (a), (b) Surface with radius $R = 5$ mm and (c), (d) flat surface; shape angle $\alpha = -24°$, $6°$, spacing $S = (0.2–0.4)$ mm, groove depth $h = H_{tc}$. Sub – substrate, BC – bond coat, TC – top coat, GL – glazed layer. (a), (c) In-plane (hoop) stress distribution. (b), (d) Out-of-plane (radial) stress distribution.

result of a stress concentration. It is worth mentioning, that the out-of-plane stresses differ for curved and flat geometry. While on an $R = 5$ mm surface, the radial stresses mainly rise with a deeper groove, bringing a risk of lateral cracking (Fig. 13, b); on a flat surface, fully cut trenches move the stresses into the compressive region in the top coat, making them somewhat safer compared to other configurations (Fig. 13, d).

As expected, the increased periodicity makes the grooving effect more prominent, because trenches are more evenly distributed in the TBC. Interestingly, that $S = 0.4$ mm spacing behaves even worse than the just glazed geometry, considering the in-plane stress relief (Fig. 14, a, c). This may be attributed to a prevalent influence of the stress concentration and induced bending in the layers, which did not exist in the case of a non-grooved geometry. Nonetheless, considering the σ_y for a curved surface (Fig. 14, b), increasing the spacing reduces the out-of-plane stresses in the top coat, even below the glazed baseline. Thus, larger S grooves may be used as mainly crack-arresting features. However, such grooves would not be advisable on flat surfaces (Fig. 14, d).

Another important aspect of the groove geometry is its shape angle α.

It was varied in the simulation from $-24°$ (the largest dove-tail groove achieved in the experiments) to $6°$ (naturally produced by a straight laser pass). Results allow seeing how the coating becomes more stress compliant with a wider groove (Fig. 15). In-plane stresses decay and approach the zero line, starting from the TC bulk, with the lowest value being for the $\alpha = -24°$ (Fig. 15, a, c). However, at the same time, the BC-TC interfacial stresses rise, which may suggest that the most likely place of failure will be the zone around TGO. And in the case of the curved geometry (Fig. 15, b), it can also occur in the TC-glazing interface due to tensile radial stress, which is less drastic as there still will be some top coat remaining.

The wider groove also relaxes the stress in the top coat closer to the BC due to the larger length of the freed interface, no longer constrained by the top coat (Fig. 15, a, c). And if in the case of a flat surface, the groove shape does not affect the glazed layer σ_x stresses, in the case of a curved surface a wider groove increases the compressive residual stress (Fig. 15, a). This happens due to the decreased stiffness of the top coat, which makes the glazed layer experience a larger portion of the deformation from the substrate, which before was partially accommodated by
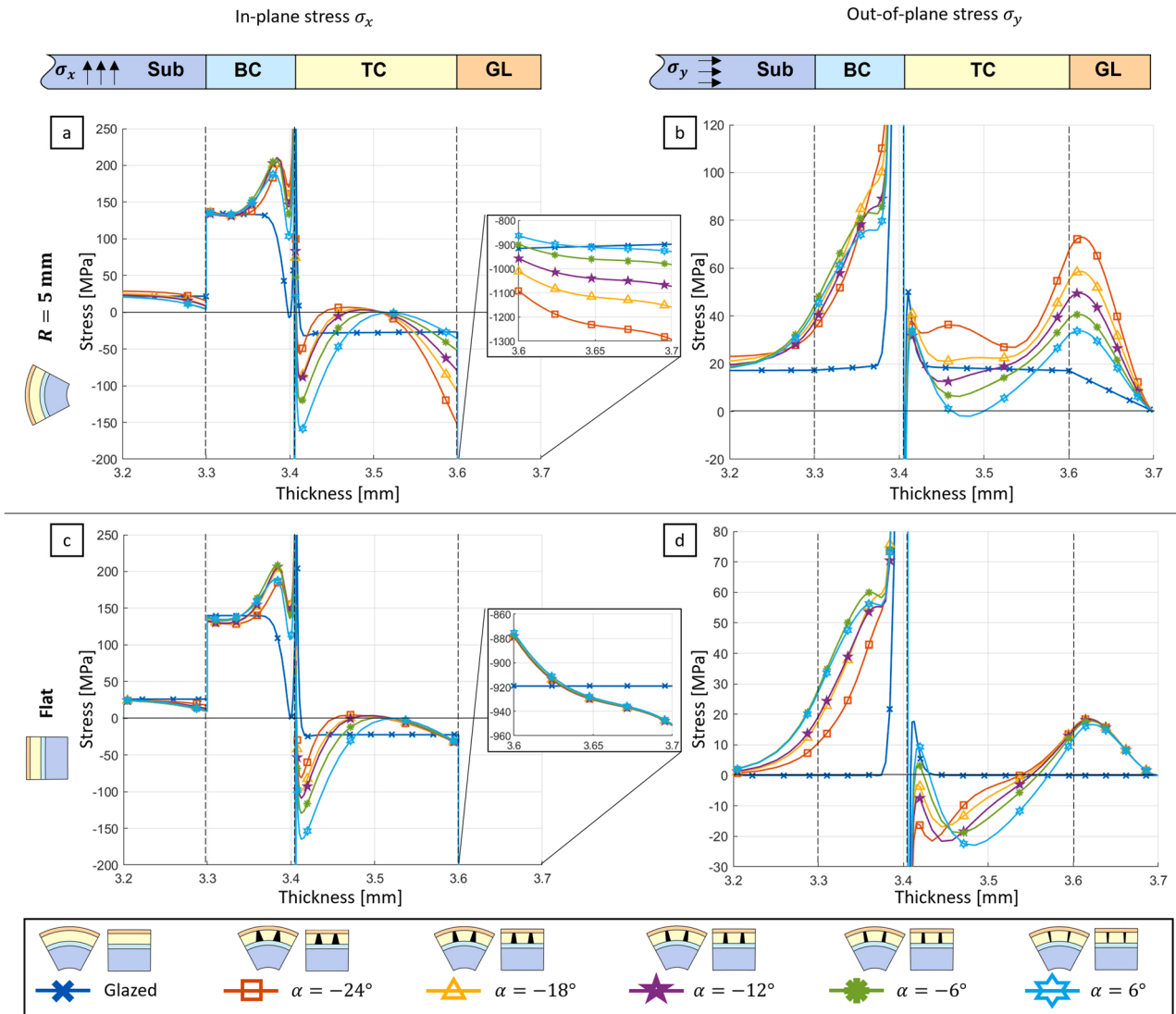
Fig. 15. The influence of **the shape angle α** on the residual stresses in the section through the middle of the pillar after 5 isothermal cycles. Markers are plotted with a 5-data points spacing. (a), (b) Surface with radius $R = 5$ mm and (c), (d) flat surface; shape angle $\alpha = (-24-6°)$, spacing $S = 0.2$ mm, groove depth $h = H_{tc}$. Sub – substrate, BC – bond coat, TC – top coat, GL – glazed layer. (a), (c) In-plane (hoop) stress distribution. (b), (d) Out-of-plane (radial) stress distribution.

the top coat. Also, it suggests that on smaller radii surfaces, the wider groove will contribute to the buckling failure, and thus its size needs to be limited. Furthermore, a larger groove induces a considerable tensile out-of-plane stress (Fig. 15, b), which only increases the risk of failure by lateral delamination. Whereas on the contrary, on flat surfaces a wider groove leads to a comparatively smaller out-of-plane stress (Fig. 15, d).

4.4. Buckling analysis of the shielded-compliant TBC

As the effect of the shielded compliance modification on the stress state of the coating is outlined, another important aspect comes into place. Even though, if the stresses exceed the ultimate strength of the top coat and the crack appears, it may not always lead to failure. However, when the delaminated area is large enough, and during the cooling of the coating the compressive stresses build up – the coating may pop up and buckle. Specifically, in the case of grooving and glazing, this phenomenon can be intensified due to increased in-plane stiffness of the glazed layer and at the same time reduced out-of-plane stiffness of the grooved region.

For the assumption in the COMSOL eigenvalue study, the TBC system

is loaded with compressive stresses, arising from it being cooled down from 1050 °C to 20 °C, while there is a 1 μm crack in the BC-TC interface with a variable length (Fig. 16, a). The probability of buckling is assessed by the critical load factor, which indicates how large the initial load needs to be for the system to become unstable. For example, a critical load factor below 1 means that the compressive stresses in TBC layers driven by thermal contraction are enough for the whole system to collapse. A variation in surface curvature shows that non-flat surfaces are less prone to buckling. For example, for surface radii of 5 and 10 mm instability does not occur at all at the given thermal load, thus, any additional anti-buckling features are not necessary (Fig. 16, b). For a flatter $R = 50$ mm surface, the critical load factor decreases significantly, though still not reaching the borderline value of 1, whereas, for the flat surface, buckling will take place when the crack achieves 15 mm width.

Even though the glazed layer provides good protection against wear and corrosion, it may increase the probability of buckling (Fig. 16, c), where thicker glazing has the highest susceptibility. Referring back to Eq. (5) it can be seen that here the thickness influence is the opposite. This can be explained by the increased compressive stresses of the full-
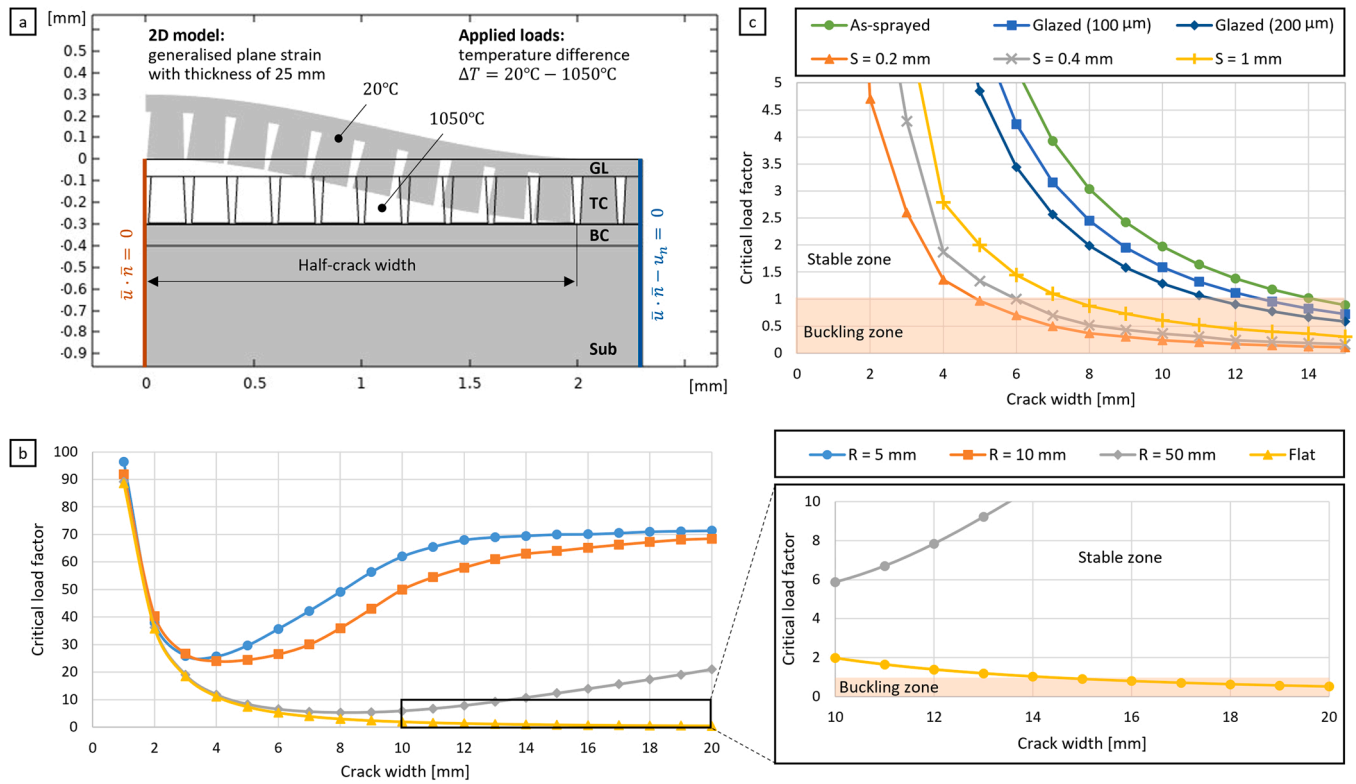
Fig. 16. Buckling analysis of the coating. (a) Model setup and mode shape. Sub – substrate, BC – bond coat, TC – top coat, GL – glazed layer. (b) Critical load factor for different surface radii of the as-sprayed geometry. (c) Critical load factor of a flat geometry with variable arrangements. Grooved samples with variable groove spacing S are represented with the following parameters: glazed layer thickness $H_{gl} = 100$ μm, shape angle $\alpha = 6°$, groove depth $h = H_{tc}$.
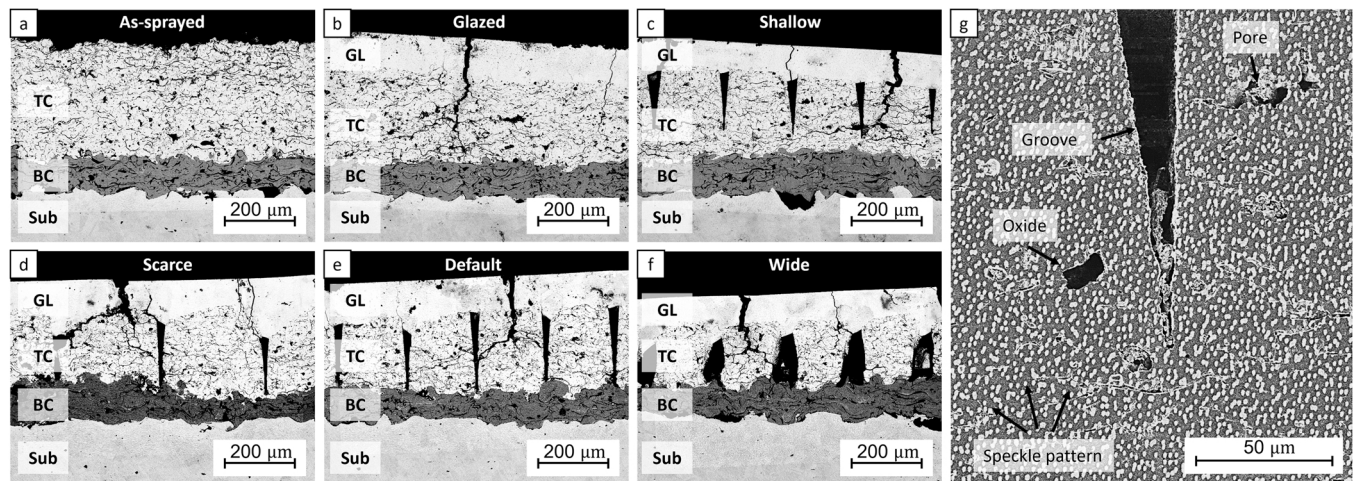

Fig. 17. BSED images of shielded-compliant samples for the in-situ digital image correlation experiment: (a) as-sprayed, (b) glazed, (c) shallow grooves, (d) scarce grooves, (e) default grooves, and (f) wide grooves. Sub – substrate, BC – bond coat, TC – top coat, GL – glazed layer. (g) FIB image of the speckle pattern of the top coat.

dense YSZ, though this effect is not very prominent as the critical crack width decreased from 13 to 11 mm for a doubled glazed thickness. However, once grooves in the top coat are made, the critical crack width decreases drastically, by more than 2-fold. At the same time, a smaller groove spacing makes the situation more adverse. It is caused by reducing the effective Young's modulus of the top coat-glazed layer by making it compliant.

This buckling study is useful in determining the size of the clusters to be made to increase the cycling life of the coating (Fig. 6). For instance, for grooving with the spacing of $S = 0.2$ mm the critical crack width is

5 mm (Fig. 16, c). This suggests, that separating the glazed layer into features smaller than 5 mm will effectively tackle the issue.

4.5. Digital image correlation of the shielded-compliant coating

Conducted FEA studies provided insight into the influence of the grooves and glazed layer on the stress state of the coating, thus, enabling a conscious design of the shielded-compliant TBC. Considering these results, several grooving shapes were picked out to be tested inside the heating stage. The as-sprayed coating was chosen as a baseline for the
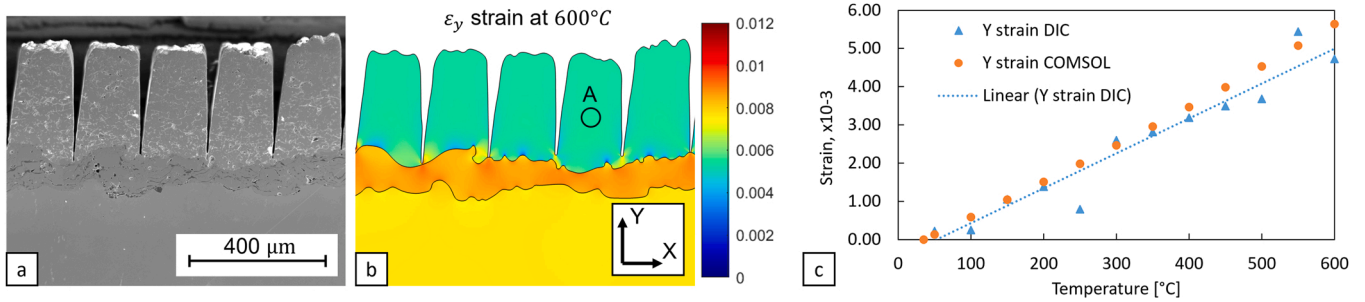
Fig. 18. Comparison of out-of-plane strain for the grooved coating. (a) SEM image of a grooved sample used in the test. (b) ε_y strain from COMSOL simulation at 600 °C. (c) ε_y strain from digital image correlation inside of circular area A.
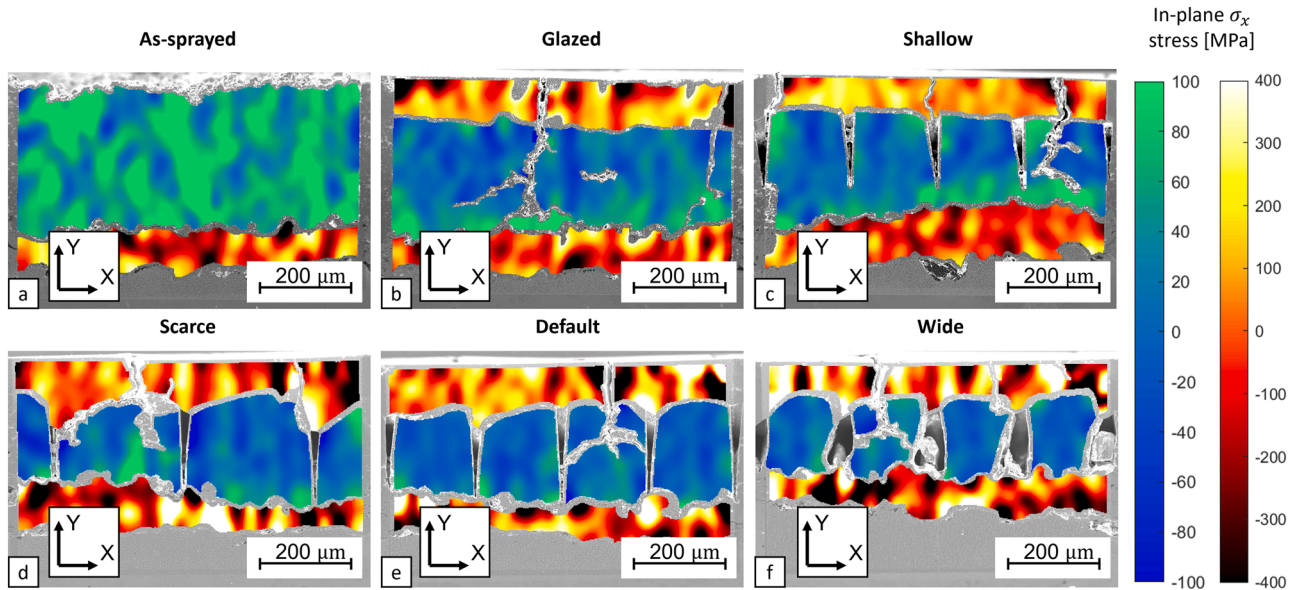

Fig. 19. In-plane (σ_x) stress maps of the TBC at 600 °C, MPa. (a) As-sprayed region. (b) Glazed-only region. (c) The region with glazing and shallow grooves. (d) The region with glazing and deep scarce grooves. (e) The region with glazing and deep grooves. (f) The region with glazing and deep wide grooves.
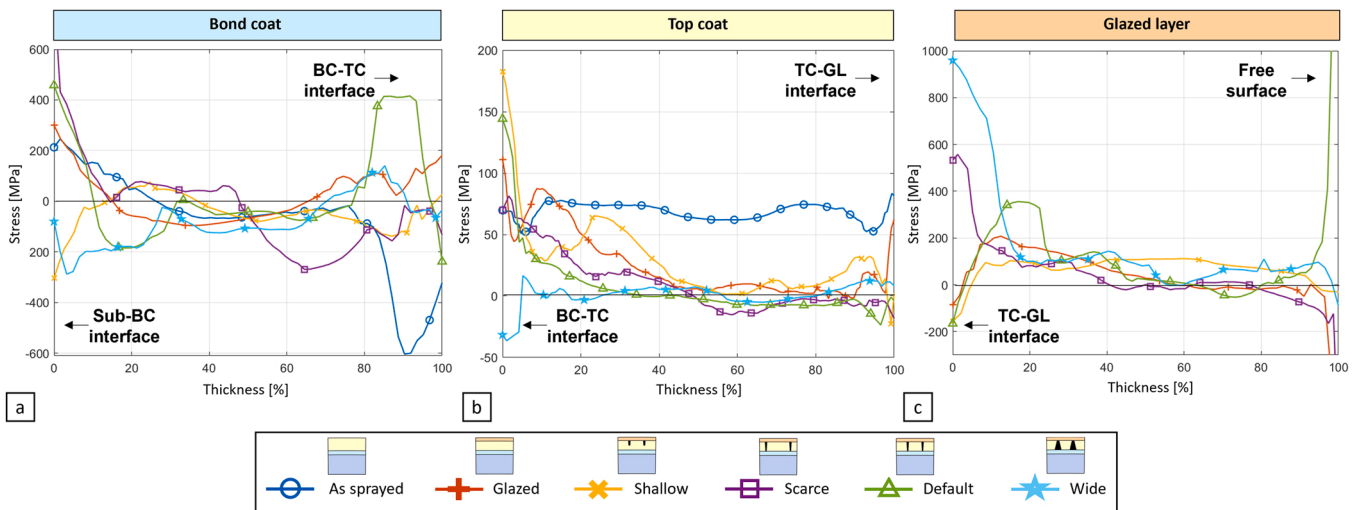

Fig. 20. In-plane (σ_x) stress of an averaged vertical cross-section along the layer thickness, MPa. Markers are plotted with a 10-data points spacing. Sub – substrate, BC – bond coat, TC – top coat, GL – glazed layer. (a) Stresses along the thickness of the bond coat with the BC-TC interface at 100% (mean STD = 231 MPa). (b) Stresses along the thickness of the top coat with the BC-TC interface at 0% (mean STD = 36 MPa). (c) Stresses along the thickness of the glazed layer with the outer surface at 100% (mean STD = 260 MPa).
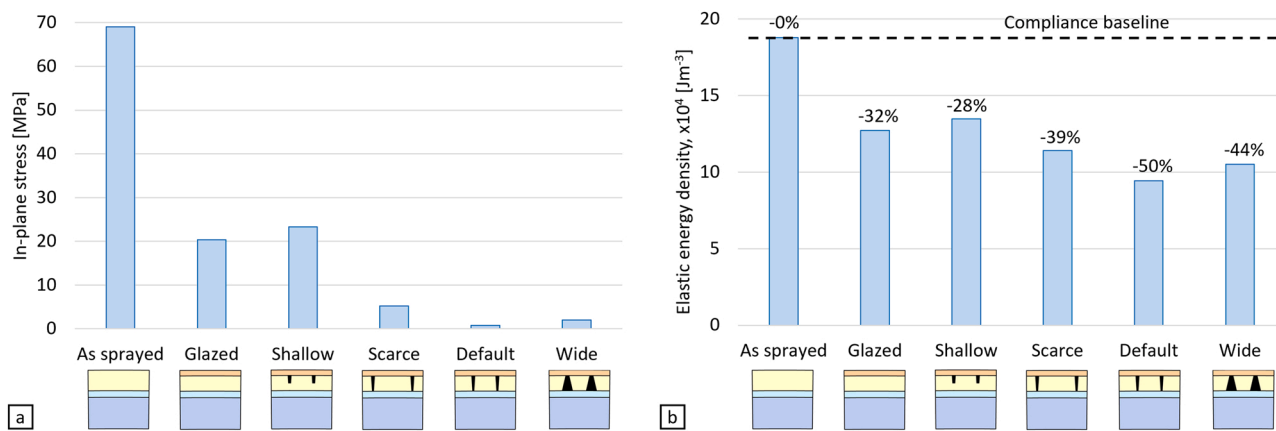
Fig. 21. Average in-plane stress and energy density of the top coat layer. (a) average in-plane (σ_x) stress for different coating structures, MPa. (b) Average elastic energy density, associated with compliance, x10^4 Jm^{-3}. The baseline indicates the level of energy for the as-sprayed sample, and the percentage denotes the reduction of the energy density for different coating structures.

Table A.1
Thermo-mechanical properties of the TBC system.

T [°C]	E [GPa]		ν		α, 10^{-6} [°C^{-1}]
		Nimonic C263 [46,47]			
21.1	221				10.3
148.9	219				11.16
204.4	212				12.06
315.6	205		0.3		12.78
426.7	198				12.96
537.8	192				13.68
648.9	185				14.22
982	143				18.1
		NiCoCrAlY [48]			
25	204				11.6
400	183		0.3		14.0
800	154				16.0
1200	118				20.8
		Al$_2$O$_3$ [49,50]			
20	400		0.23		8
200	390		0.23		8.2
400	380		0.24		8.4
600	370		0.24		8.7
800	355		0.25		9
1000	325		0.25		9.3
1100	320		0.25		9.6
		8%-wt. YSZ [49,51,52]			
	APS	Glazed	APS	Glazed	
20	48		0.1		9
200	47		0.1		9.2
400	44		0.1		9.6
600	40	205	0.11	0.23	10.1
800	34		0.11		10.8
1000	26		0.12		11.7
1100	22		0.12		12.2

Table A.2
Yield strength of the bond coat and TGO [53,54].

T [°C]	σ_{yield} [MPa]	
	NiCoCrAlY	Al$_2$O$_3$
20	850	8000
300	850	
500		8000
750	74	
1000	74	300
1100		300

Table A.3
Creep properties for the layers of the TBC [55].

Material	T [°C]	A [MPa^{-n} s^{-1}]	n
	≤600	6.54·10^{-19}	4.57
NiCoCrAlY	700	2.2·10^{-12}	2.99
	800	1.84·10^{-7}	1.55
	≥850	2.15·10^{-8}	2.45
Al$_2$O$_3$	1000	7.3·10^{-12}	1
8%-wt. YSZ	1000	1.8·10^{-10}	1

comparison; glazed coating was made to highlight its effect on the stress state of the system and to show how additional grooving alters it. As wide negatively tapered grooves were shown by FEA to provide the highest compliance for a flat surface, trenches with the shape angle $\alpha = -24°$ and spacing $S = 0.2$ mm were manufactured. A larger negative angle or smaller spacing appeared to be too complicated to produce as on cooling of the glazing stage massive contraction of the dense layer drives delamination of the coating. Potentially it may be eliminated by external heating of the TBC to reduce thermal gradients and thus, cooling stresses.

Six different areas were chosen to understand the influence of separate modification parameters – groove depth, spacing, and width (shape angle). The as-sprayed coating (Fig. 17, a) is presented by a porous structure, containing small microcracks, due to the spraying process. After laser remelting, the glazed layer induces vertical cracking on the cooling stage due to the contraction of the remelt (Fig. 17, b). Even though the density of the layer increases the Young's modulus, which should promote higher in-plane stresses of the coating, vertical cracks will provide some relief to the thermal mismatch.

Grooved samples show similar structures (Fig. 17, c-f), where the glazing also induces vertical cracks. Only for larger spacing grooves (Fig. 17, d), this remelted layer has a variation in thickness as thermal conduction conditions change. During laser remelting, the top coat starts to heat up progressively, thus the glazing thickness is smaller at the beginning of the pillar. But at its end, enough heat is accumulated to melt the coating deeper. All the other grooved samples show a constant thickness of the glazed layer, which is expected to promote even conditions of abrasive wear and thermal contraction. Each sample was engraved with a speckle pattern, consisting of randomised dots of 1 μm size to achieve stable indexing in the DIC software (Fig. 17, g).

In order to see how digital image correlation analysis performs on a candidate grooved sample and to calibrate the model, it was gradually heated in the SEM. Its geometry was copied and recreated in COMSOL to compare with the DIC results for the reference temperature of 23 °C
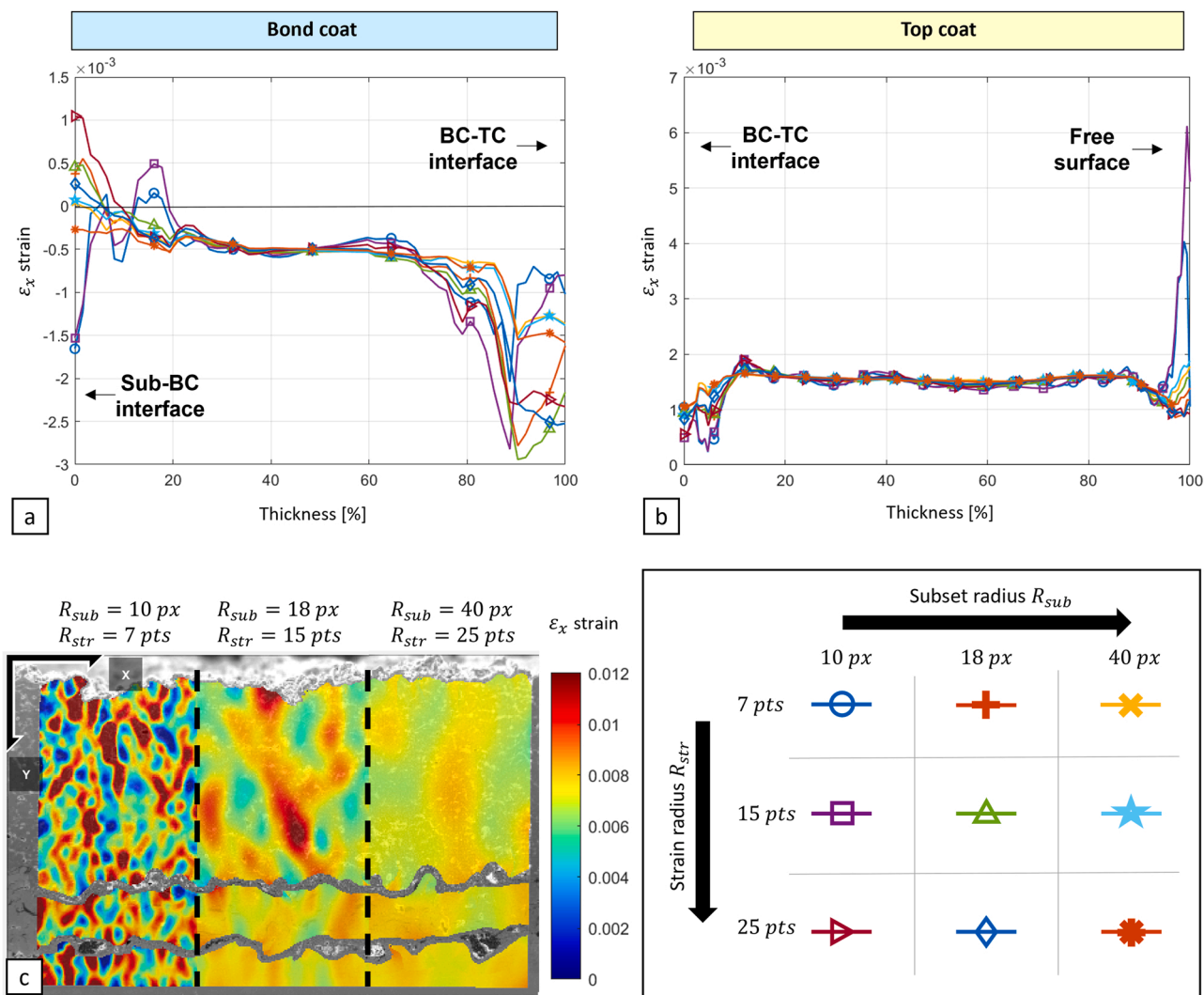
Fig. A1. In-plane (ε_x) strain in the TBC system at 600 °C when varying the subset radius R_{sub} and the strain radius R_{str}. SEM images had a resolution of 1280 x 1024 pixels. Markers are plotted with a 10-data points spacing. Sub – substrate, BC – bond coat, TC – top coat. (a) An averaged vertical cross-section along the thickness of the bond coat. (b) An averaged vertical cross-section along the thickness of the top coat. (c) Strain map, used for cross-sections (a) and (b). The effect of noise reduction by smoothing is shown.

(Fig. 18, a, b). As it is seen, the out-of-plane strain in the coating is equalised in the bulk, but due to the BC-TC interface asperities, it varies closer to the bond coat, increasing in bottoms and decreasing in tops (Fig. 18, b). Considering this, area A, distanced from the interface was chosen and its averaged strain is plotted alongside the same area from DIC (Fig. 18, c). The results show a good correspondence between the simulation and the DIC. However, some variations of the DIC strain are visible, these are the result of analysis of the unspeckled surface, using only the morphological features of the coating.

Since thermal mismatch takes place along the interface of the materials, it will mainly affect the in-plane stress. Thus, it is the σ_x stress, which was used to evaluate the effect of grooving and glazing on the coating stress state at elevated temperatures (Fig. 19).

For the as-sprayed coating (Fig. 19, a) the stress field appears more or less homogeneous, showing an average of 69 MPa. Variations on the maps arise from the coating's imperfections – pores and cracks, which cause smaller or larger strains in DIC. However, as soon as the coating is laser machined, its stress state is drastically changed.

Vertical crack after glazing already seems to provide a significant relaxation in the mismatch (Fig. 19, b). Overall bulk stress is reduced, showing local bursts only in cracked and interfacial areas. A similar effect is noticeable in the shallowly grooved sample (Fig. 19, c), where

the thermally-induced stress relief takes place only in the grooving area, but below stresses are higher. This means, that having a groove, which does not go to the interface, brings in a stress concentrator at its tip. Even though, it may considerably reduce the coating cycling life, as the crack could initiate and potentially branch into the horizontal plane, delamination of the pillars will still leave some top coat below. When in the case of deep grooves (Fig. 19, d-f) this could cause a complete spallation of the entire coating.

In the case of the default and wide grooves (Fig. 19, e, and f), the bulk stress state looks similar, and in comparison to the as-sprayed coating – it is relieved almost completely. Only at the BC-TC interface, some bursts are noticeable due to the asperities.

To better visualise the coating stress state and compare the influence of the coating micro-features, an average vertical (along Y) cross-section was calculated (Fig. 20). As the thicknesses of the layers differ across the sample, stress values were plotted against normalised thicknesses from 0% to 100% for three layers – bond and top coat, and glazing.

At the bond coat area (Fig. 20, a) all of the coatings show similar behaviour, with mostly compressive stress in the bulk, due to the higher CTE compared to the ceramic coating. Adding grooves or a crack as in the case of the glazed sample moves the stress to the tensile region. In general terms, it is not favourable as tensile stresses tend to be the main

in the crack nucleation process. A similar trend is visible in the glazed layer (Fig. 20, c). It presents some stress in the bulk, which is a result of an increased Young's modulus, however closer to the top coat interface the values are increased. This is associated with the fact that compliance features influence becomes more prominent farther away from the interface. High values of the standard deviation in the layers are an inevitable result of rich natural microstructures – porosity, splat structure and oxides. Such points may produce large out-of-mean figures, however averaging procedure allows for eliminating their presence.

The top coat section perfectly reflects the grooving influence (Fig. 20, b). The as-sprayed sample shows a more or less constant value of the in-plane stress because the underlying bond coat pulls it evenly. The crack, introduced by the glazed layer, seems to be an already effective stress-relieving feature. The σ_x stress decays more and more when distancing from the bond coat, as the top coat becomes free to expand with its own CTE. Introducing grooves allows for making the relaxation more extensive, due to their periodicity throughout the coating. Shallow grooves reduce stresses only in the machined area, and their effect is less visible compared to the just glazed area. This may be explained by the long glazed crack which induces a stronger relaxation, compared to a shallow groove. However, cracking due to remelting is not a very controllable process, whereas having accurate trenches allows for achieving stable compliance throughout the surface.

The influence of the spacing is visible from the scarce ($S = 0.3$ mm) and default ($S = 0.2$ mm) grooves. Even though the relaxation of the bulk is comparable in values, the smaller spacing provides a much more rapid decay to the zero stress line as in the FEA result (Fig. 14, c), which is expected to enable a longer cycling life for the coating. In the case of the wide grooves ($\alpha = -24°$), this decay is almost instant, showing smaller interfacial stress. Similar findings are shown in Fig. 15, c. The reason behind this fact is the reduced contact length of the interface, which lowers the pulling strains arising from the bond coat's larger expansion.

A summary of the σ_x stress states is shown in Fig. 21, a. The average in-plane stress is going down for the shielded-compliant samples, with the default and wide grooves almost approaching zero, showing excellent mismatch relief. As the main aim of the coating structures is to increase thermal compliance, it may be assessed through the elastic energy density (Fig. 21, b). The higher energy values mean that the coating develops larger stress at a given strain (low compliance), and this energy may be used for crack nucleation and propagation. Thus, it is beneficial to have low energy, which is not sufficient for the creation of free surfaces in the cracking process. The elastic energy density is defined by the following expression, considering YZ and XZ components equal to zero as for the used 2D approximation:

$$u = 0.5(\varepsilon_x \cdot \sigma_x + \varepsilon_y \cdot \sigma_y + \varepsilon_z \cdot \sigma_z + \varepsilon_{xy} \cdot \tau_{xy}) \; [\text{Jm}^{-3}], \tag{12}$$

Considering the as-sprayed coating to be a zero compliance level, the addition of cracks or grooves leads to higher compliance. Glazed, shallow, and scarce samples reduce the energy almost by a third, whereas default and wide grooves almost by a half. Compliance of the scarce grooves is considerably lower than for just glazed or shallowly grooved areas, which indicates the high importance of periodicity and larger depths of the trenches. Even being close to each other, higher compliance of the default sample (50%) compared to the wide grooves (44%) may be explained by more even deformation conditions of the coating, as the wide dove-tail trenches can induce some additional out-of-plane stresses leading to an increase of the elastic energy.

5. Conclusion

A post-deposition laser modification for thermal barrier coatings is a promising way of increasing the performance of a range of coated components. The shielded compliance approach, proposed in the paper, is targeting different aspects of the coating operational factors. Grooves

in the top coat reduce thermal mismatch, releasing the stresses arising from the high-temperature exposures. At the same time, cracks, initiating in the coating, could be arrested within the segmented part, hindering their propagation. A glazed layer, covering the grooved top coat, protects the TBC from abrasive wear, hot gas, and CMAS infiltration by providing a hard and dense barrier against environmental factors. Such a combined system can be tailored and adjusted for specific operational conditions (temperatures, surface curvatures), giving a flexible framework for controlling the coating's compliance.

In general, laser-machined structures show a few defects. However, even though the thermal diffusion length is limited for the picosecond pulses, the measured damaged area was about 10 μm deep. This result refers to plasma pressure waves being the cause rather than heat dissipation. The remelted layer showed a significantly altered, almost stress-free microstructure, represented by large and elongated grains which imply additional thermal compliance. Moreover, a tilt of the zirconia unit cells towards the laser scanning direction may allow tailoring the glazing layer for specific needs, considering the YSZ anisotropy.

The conducted FEA study showed the general trend of increasing the compliance for the tighter-spaced, deeper, and wider grooves, reducing the residual stresses after cycling. However, on curved surfaces narrower grooves are advised, because of out-of-plane stresses in BC-TC interfaces. As another aspect of the modification, introducing grooves into the system can cause buckling with much smaller delamination sizes than for glazed or as-sprayed geometry, making the modified coating highly vulnerable. However, limiting the critical cracking length through coating segmentation determined from FEA allows for tackling this issue.

To support the conclusions from the FEA and provide a tool for assessing the performance of the produced arrangements (grooves and glazing), an SEM in-situ heating test with subsequent digital image correlation was proposed and conducted. The strains at elevated temperatures were converted to stress which was used as a measure of the final assessment. The coating develops tensile in-plane stress of 69 MPa (at 600 °C), whereas modified samples show a significant stress-relieving effect. Glazing-induced cracks already appear to be good compliance features, however, controlled grooves show a more stable and reliable result due to their periodicity. As expected, the highest compliance was achieved by providing tighter-spaced deep grooves, with average in-plane stress of almost zero. Nonetheless, despite not being the most compliant, the wide grooves ($\alpha = -24°$) show the most rapid decay in the in-plane stresses, decreasing the interfacial stresses.

The concept presented in the study is not limited to the considered example of APS YSZ. It can be expanded to any other applications of coatings, which can benefit from increased compliance and/or environmental protection. This may improve the lifespan of components or enable them to withstand operational conditions not achievable before.

Declaration of Competing Interest

The authors declare that they have no known competing financial interests or personal relationships that could have appeared to influence the work reported in this paper.

Appendix

Thermally-induced stress in a multi-layered cylinder

Radial displacement of any point on the cylinder:

$$u_i(r) = \frac{1 + \nu_i(r)}{1 - \nu_i(r)} \cdot \frac{\alpha_i(r)}{r} \int_{R_i}^{r} \Delta T_i(r) \cdot r \cdot dr + A_i r + \frac{B_i}{r} \ [m], \tag{A.1}$$

where A_i and B_i are constants found from boundary conditions, $\nu_i(r)$ – Poisson's ratio, $\alpha_i(r)$ – coefficient of thermal expansion of the i-th layer [°C^{-1}], $\Delta T_i(r)$ – temperature difference defined as:

$$\Delta T_i(r) = T_i(r) - T_i^* \ [°C], \tag{A.2}$$

Where $T_i(r)$ – temperature of the point on the radius r [°C], T_i^* - reference temperature for i-th layer [°C].

Radial and hoop stresses can be calculated from:

$$\sigma_{r_i}(r) = -\frac{E_i(r)\alpha_i(r)}{1 - \nu_i(r)} \cdot \frac{1}{r^2} \cdot \int_{R_i}^{r} \Delta T_i(r) \cdot r dr + \frac{E_i(r)}{(1 + \nu_i(r)) \cdot (1 - 2\nu_i(r))} \cdot A_i - \frac{E_i(r)}{1 + \nu_i(r)} \cdot B_i \cdot \frac{1}{r^2} \ [Pa]; \tag{A.3}$$

$$\sigma_{h_i}(r) = \frac{E_i(r)\alpha_i(r)}{1 - \nu_i(r)} \cdot \frac{1}{r^2} \cdot \int_{R_i}^{r} \Delta T_i(r) \cdot r dr + \frac{E_i(r)}{(1 + \nu_i(r)) \cdot (1 - 2\nu_i(r))} \cdot A_i + \frac{E_i(r)}{1 + \nu_i(r)} \cdot B_i \cdot \frac{1}{r^2} - \frac{E_i(r)\alpha_i(r)}{1 - \nu_i(r)} \cdot \Delta T_i(r) \ [Pa], \tag{A.4}$$

where $E_i(r)$ – Young's modulus [Pa].

For boundary conditions, the continuity of displacements and radial stresses on layer interfaces as well as pressures (if any are present) on external surfaces are applied:

$$\begin{cases} u_i(R_{i+1}) = u_{i+1}(R_{i+1}), & i = 1 \ldots n - 1 \\ \sigma_{r_i}(R_{i+1}) = \sigma_{r_{i+1}}(R_{i+1}), & i = 1 \ldots n - 1 \\ \sigma_{r_1}(R_1) = p_1 \\ \sigma_{r_n}(R_{n+1}) = p_2 \end{cases} \tag{A.5}$$

Introducing the following notation:

$$f_i(r) = \int_{R_1}^{r} \Delta T_i(r) \cdot r dr;$$

$$W_i(r) = \frac{(1 + \nu_i(r)) \cdot \alpha_i(r)}{1 - \nu_i(r)};$$

$$X_i(r) = -\frac{E_i(r)\alpha_i(r)}{1 - \nu_i(r)}; \tag{A.6}$$

$$Y_i(r) = \frac{E_i(r)}{(1 + \nu_i(r)) \cdot (1 - 2\nu_i(r))};$$

$$Z_i(r) = -\frac{E_i(r)}{1 + \nu_i(r)}.$$

Finally, to calculate the constants the following system of linear equations needs to be solved:

$$\begin{cases} W_1(R_2)f_1(R_2) + R_2^2 A_1 + B_1 = W_2(R_2)f_2(R_2) + R_2^2 A_2 + B_2 \\ \quad \vdots \\ W_{n-1}(R_n)f_{n-1}(R_n) + R_n^2 A_{n-1} + B_{n-1} = W_n(R_n)f_n(R_n) + R_n^2 A_n + B_n \\ X_1(R_2) \cdot f_1(R_2) + R_2^2 \cdot Y_1(R_2) \cdot A_1 + Z_1(R_2) \cdot B_1 = X_2(R_2) \cdot f_2(R_2) + R_2^2 \cdot Y_2(R_2) \cdot A_2 + Z_2(R_2) \cdot B_2 \\ \quad \vdots \\ X_{n-1}(R_n) \cdot f_{n-1}(R_n) + R_n^2 \cdot Y_{n-1}(R_n) \cdot A_{n-1} + Z_{n-1}(R_n) \cdot B_{n-1} = X_n(R_n) \cdot f_n(R_n) + R_n^2 \cdot Y_n(R_n) \cdot A_n + Z_n(R_n) \cdot B_n \\ X_1(R_1)f_1(R_1) + R_1^2 \cdot Y_1(R_1) \cdot A_1 + Z_1(R_1) \cdot B_1 = R_1^2 \cdot p_1 \\ X_n(R_{n+1})f_n(R_{n+1}) + R_{n+1}^2 \cdot Y_n(R_{n+1}) \cdot A_n + Z_n(R_{n+1}) \cdot B_n = R_{n+1}^2 \cdot p_2 \end{cases} \tag{A.7}$$

FEA material thermo-mechanical properties

See appendix Table A1, A2 and A3.

DIC parameters sensitivity study

See appendix Fig. A1

References

[1] J.G. Thakare, C. Pandey, M.M. Mahapatra, R.S. Mulik, Thermal barrier coatings—a state of the art review, 2020 27, Met. Mater. Int. 7 (27) (2020) 1947–1968, https://doi.org/10.1007/S12540-020-00705-W.

[2] D.R. Clarke, M. Oechsner, N.P. Padture, Thermal-barrier coatings for more efficient gas-turbine engines, MRS Bull. 37 (2012) 891–898, https://doi.org/10.1557/MRS.2012.232.

[3] W.R. Chen, X. Wu, D. Dudzinski, P.C. Patnaik, Modification of oxide layer in plasma-sprayed thermal barrier coatings, Surf. Coat. Technol. 200 (2006) 5863–5868, https://doi.org/10.1016/J.SURFCOAT.2005.08.141.

[4] A.C. Karaoglanli, H. Dikici, Y. Kucuk, Effects of heat treatment on adhesion strength of thermal barrier coating systems, Eng. Fail Anal. 32 (2013) 16–22, https://doi.org/10.1016/J.ENGFAILANAL.2013.02.029.

[5] J.A. Thompson, T.W. Clyne, The effect of heat treatment on the stiffness of zirconia top coats in plasma-sprayed TBCs, Acta Mater. 49 (2001) 1565–1575, https://doi.org/10.1016/S1359-6454(01)00065-9.

[6] K.A. Khor, Z.L. Dong, Y.W. Gu, Plasma sprayed functionally graded thermal barrier coatings, Mater. Lett. 38 (1999) 437–444.

[7] A. Bhattacharyya, D. Maurice, Residual stresses in functionally graded thermal barrier coatings, Mech. Mater. 129 (2019) 50–56.

[8] T. Samani, M. Kermani, M. Razavi, M. Farvizi, I. Mobasherpour, A comparative study on the microstructure, hot corrosion behavior and mechanical properties of duplex and functionally graded nanostructured/conventional YSZ thermal barrier coatings, Mater. Res Express 6 (2019), https://doi.org/10.1088/2053-1591/ab4956.

[9] M. Guven Gok, G. Goller, Production and characterisation of GZ/CYSZ alternative thermal barrier coatings with multilayered and functionally graded designs, J. Eur. Ceram. Soc. 36 (2016) 1755–1764, https://doi.org/10.1016/J.JEURCERAMSOC.2016.01.036.

[10] X. Song, Y. Xu, Y. Ding, J. Zhang, X. Guo, C. Jiang, W. Zheng, Y. Zeng, Study of microstructure, electronic structure and thermal properties of Al2O3-doped tetragonal YSZ coatings, Appl. Surf. Sci. 542 (2021), https://doi.org/10.1016/J.APSUSC.2020.148553.

[11] S.L. Jiang, X. Huang, Z. He, Phase transformation and lattice parameter changes of trivalent rare earth doped YSZ as a function of temperature, J. Mater. Eng. Perform. 25 (2016) 4686–4694, https://doi.org/10.1007/s11665-016-2328-5.

[12] A. Rauf, Q. Yu, L. Jin, C. Zhou, Microstructure and thermal properties of nanostructured lanthana-doped yttria-stabilized zirconia thermal barrier coatings by air plasma spraying, Scr. Mater. 66 (2012) 109–112, https://doi.org/10.1016/j.scriptamat.2011.10.017.

[13] J.L. Smialek, Improved oxidation life of segmented plasma sprayed 8YSZ thermal barrier coatings, J. Therm. Spray. Technol. 13 (2004) 66–75, https://doi.org/10.1007/S11666-004-0051-5.

[14] Y. Wang, H. Guo, S. Gong, Thermal shock resistance and mechanical properties of La2Ce2O7 thermal barrier coatings with segmented structure, Ceram. Int 35 (2009) 2639–2644, https://doi.org/10.1016/J.CERAMINT.2009.02.025.

[15] Z. Yan, L. Guo, Z. Li, Y. Yu, Q. He, Effects of laser glazing on CMAS corrosion behavior of Y2O3 stabilized ZrO2 thermal barrier coatings, Corros. Sci. 157 (2019) 450–461, https://doi.org/10.1016/J.CORSCI.2019.06.025.

[16] L. Guo, Y. Gao, Y. Cheng, J. Sun, F. Ye, L. Wang, Microstructure design of the laser glazed layer on thermal barrier coatings and its effect on the CMAS corrosion, Corros. Sci. 192 (2021), 109847, https://doi.org/10.1016/J.CORSCI.2021.109847.

[17] P.C. Tsai, J.H. Lee, C.L. Chang, Improving the erosion resistance of plasma-sprayed zirconia thermal barrier coatings by laser glazing, Surf. Coat. Technol. 202 (2007) 719–724, https://doi.org/10.1016/J.SURFCOAT.2007.07.005.

[18] C. Zhao, M. Zhao, M. Shahid, M. Wang, W. Pan, Restrained TGO growth in YSZ/NiCrAlY thermal barrier coatings by modified laser remelting, Surf. Coat. Technol. 309 (2017) 1119–1125, https://doi.org/10.1016/J.SURFCOAT.2016.05.015.

[19] M.Y. He, J.W. Hutchinson, A.G. Evans, Simulation of stresses and delamination in a plasma-sprayed thermal barrier system upon thermal cycling, Mater. Sci. Eng.: A 345 (2003) 172–178, https://doi.org/10.1016/S0921-5093(02)00458-6.

[20] R. Panat, S. Zhang, K.J. Hsia, Bond coat surface rumpling in thermal barrier coatings, Acta Mater. 51 (2003) 239–249, https://doi.org/10.1016/S1359-6454(02)00395-6.

[21] F. Traeger, M. Ahrens, R. Vaßen, D. Stöver, A life time model for ceramic thermal barrier coatings, Mater. Sci. Eng.: A 358 (2003) 255–265, https://doi.org/10.1016/S0921-5093(03)00300-9.

[22] W. Qian, J. Cai, Z. Xin, Y. Ye, F. Dai, Y. Hua, Femtosecond laser polishing with high pulse frequency for improving performance of specialised aerospace material systems: MCrAlY coatings in thermal barrier coating system, Int J. Mach. Tools Manuf. 182 (2022), 103954, https://doi.org/10.1016/J.IJMACHTOOLS.2022.103954.

[23] S.R. Dhineshkumar, M. Duraiselvam, S. Natarajan, S.S. Panwar, T. Jena, M.A. Khan, Enhancement of strain tolerance of functionally graded LaTi2Al9O19 thermal barrier coating through ultra-short pulse based laser texturing, Surf. Coat. Technol. 304 (2016) 263–271, https://doi.org/10.1016/J.SURFCOAT.2016.07.018.

[24] M.A. Khan, M. Duraiselvam, S.S. Panwar, T. Jena, S.R. Dhineshkumar, Thermo-mechanical characterization of laser textured LaMgAl11O19/YSZ functionally graded thermal barrier coating, Surf. Coat. Technol. 321 (2017) 146–155, https://doi.org/10.1016/J.SURFCOAT.2017.04.070.

[25] H. Chen, Y. Hao, H. Wang, W. Tang, Analysis of the microstructure and thermal shock resistance of laser glazed nanostructured zirconia TBCs, : J. Therm. Spray. Technol. (2010) 558–565, https://doi.org/10.1007/s11666-009-9463-6.

[26] Z. Fan, K. Wang, X. Dong, W. Duan, X. Mei, W. Wang, J. Cui, J. Lv, Influence of columnar grain microstructure on thermal shock resistance of laser re-melted ZrO2–7 wt% Y2O3 coatings and their failure mechanism, Surf. Coat. Technol. 277 (2015) 188–196, https://doi.org/10.1016/J.SURFCOAT.2015.07.036.

[27] D. Liu, S.T. Kyaw, P.E.J. Flewitt, M. Seraffon, N.J. Simms, M. Pavier, I.A. Jones, Residual stresses in environmental and thermal barrier coatings on curved superalloy substrates: Experimental measurements and modelling, Mater. Sci. Eng. A 606 (2014) 117–126, https://doi.org/10.1016/j.msea.2014.03.014.

[28] M. Song, Y. Ma, S.-K. Gong, Analysis of residual stress distribution along interface asperity of thermal barrier coating system on macro curved surface, Prog. Nat. Sci.: Mater. Int. 21 (2011) 262–267.

[29] X. Guo, W. Sun, A. Becker, A. Morris, M. Pavier, P. Flewitt, M. Tierney, C. Wales, Thermal and stress analyses of a novel coated steam dual pipe system for use in advanced ultra-supercritical power plant, Int. J. Press. Vessels Pip. 176 (2019), https://doi.org/10.1016/j.ijpvp.2019.103933.

[30] V. Maurel, E.P. Busso, J. Frachon, J. Besson, F. N'Guyen, A methodology to model the complex morphology of rough interfaces, Int J. Solids Struct. 51 (2014) 3293–3302, https://doi.org/10.1016/J.IJSOLSTR.2014.04.015.

[31] S.R. Choi, J.W. Hutchinson, A.G. Evans, Delamination of multilayer thermal barrier coatings, Mech. Mater. 31 (1999) 431–447, https://doi.org/https://doi.org/10.1016/S0167-6636(99)00016-2.

[32] C. Bumgardner, B. Croom, X. Li, High-temperature delamination mechanisms of thermal barrier coatings: In-situ digital image correlation and finite element analyses, Acta Mater. 128 (2017) 54–63, https://doi.org/10.1016/J.ACTAMAT.2017.01.061.

[33] D. Zhang, X.M. Zhang, G.C. Nie, Z.Y. Yang, H. Ding, Characterization of material strain and thermal softening effects in the cutting process, Int J. Mach. Tools Manuf. 160 (2021), 103672, https://doi.org/10.1016/J.IJMACHTOOLS.2020.103672.

[34] J. Blaber, B. Adair, A. Antoniou, Ncorr: open-source 2D digital image correlation matlab software, Exp. Mech. 55 (2015) 1105–1122, https://doi.org/10.1007/s11340-015-0009-1.

[35] X.C. Zhang, B.S. Xu, H.D. Wang, Y.X. Wu, An analytical model for predicting thermal residual stresses in multilayer coating systems, Thin Solid Films 488 (2005) 274–282, https://doi.org/10.1016/J.TSF.2005.04.027.

[36] K. Winter, Z. Liao, R. Ramanathan, D. Axinte, G. Vakil, C. Gerada, How non-conventional machining affects the surface integrity and magnetic properties of non-oriented electrical steel, Mater. Des. 210 (2021), 110051, https://doi.org/10.1016/J.MATDES.2021.110051.

[37] A. la Monaca, D.A. Axinte, Z. Liao, R. M'Saoubi, M.C. Hardy, Towards understanding the thermal history of microstructural surface deformation when cutting a next generation powder metallurgy nickel-base superalloy, Int J. Mach. Tools Manuf. 168 (2021), 103765, https://doi.org/10.1016/J.IJMACHTOOLS.2021.103765.

[38] Z. Liao, A. la Monaca, J. Murray, A. Speidel, D. Ushmaev, A. Clare, D. Axinte, R. M'Saoubi, Surface integrity in metal machining - Part I: Fundamentals of surface characteristics and formation mechanisms, Int J. Mach. Tools Manuf. 162 (2021), 103687, https://doi.org/10.1016/J.IJMACHTOOLS.2020.103687.

[39] A. Tünnermann, B. Wellegehausen, B.N. Chichkov, C. Momma, H. Jacobs, H. Welling, S. Nolte, Ablation of metals by ultrashort laser pulses, J. Opt. Soc. Am. B 14 (1997) 2716–2722, https://doi.org/10.1364/JOSAB.14.002716.

[40] A. Heiming, W. Petry, J. Trampenau, W. Miekeley, J. Cockcroft, The temperature dependence of the lattice parameters of pure BCC Zr and BCC Zr-2 at%Co, J. Phys.: Condens. Matter 4 (1992) 727–733.

[41] J. Liu, X. Zhang, Y. He, Z. Zhao, M. Xia, Y. Hu, Suspended water droplet confined laser shock processing at elevated temperatures, Int J. Mach. Tools Manuf. 179 (2022), 103917, https://doi.org/10.1016/J.IJMACHTOOLS.2022.103917.

[42] A. la Monaca, J.W. Murray, Z. Liao, A. Speidel, J.A. Robles-Linares, D.A. Axinte, M.C. Hardy, A.T. Clare, Surface integrity in metal machining - Part II: Functional performance, Int J. Mach. Tools Manuf. 164 (2021), 103718, https://doi.org/10.1016/J.IJMACHTOOLS.2021.103718.

[43] D. Axinte, H. Huang, J. Yan, Z. Liao, What micro-mechanical testing can reveal about machining processes, Int J. Mach. Tools Manuf. 183 (2022), 103964, https://doi.org/10.1016/J.IJMACHTOOLS.2022.103964.

[44] L. Zhang, J. Vleugels, L. Darchuk, O. van der Biest, Magnetic field oriented tetragonal zirconia with anisotropic toughness, J. Eur. Ceram. Soc. 31 (2011) 1405–1412, https://doi.org/10.1016/J.JEURCERAMSOC.2011.02.002.

[45] D. Ushmaev, Z. Liao, A. Norton, D. Axinte, On the importance of interface stability in cellular automata models: Planar and dendritic solidification in laser melted YSZ, Mater. Des. 219 (2022), 110823, https://doi.org/10.1016/J.MATDES.2022.110823.

[46] Alloy C263 - Specialty Cobalt Alloys from NeoNickel, (2022). https://www.neonickel.com/alloys/nickel-alloys/alloy-c263/ (accessed November 12, 2022).

[47] A.K. Ray, N. Roy, B. Dash, D.K. Das, V.R. Ranganath, B. Goswami, M.P. Singh, Y.N. Tiwari, P.K. Roy, H.K. Das, D. Sanyal, E.S. Dwarakadasa, High temperature mechanical properties of thermal barrier coated superalloy applied to combustor liner of aero engines, High. Temp. Mater. Process. 25 (2006) 109–119, https://doi.org/10.1515/HTMP.2006.25.3.109/MACHINEREADABLECITATION/RIS.

[48] S. Widjaja, A.M. Limarga, T.H. Yip, Modeling of residual stresses in a plasma-sprayed zirconia/alumina functionally graded-thermal barrier coating, Thin Solid Films 434 (2003) 216–227, https://doi.org/10.1016/S0040-6090(03)00427-9.

[49] C. Zhou, N. Wang, H. Xu, Comparison of thermal cycling behavior of plasma-sprayed nanostructured and traditional thermal barrier coatings, Mater. Sci. Eng. A. 452– 453 (2007) 569–574, https://doi.org/10.1016/J.MSEA.2006.11.027.

[50] Aluminum Oxide Al2O3 Material Properties, (2022). https://accuratus.com/alumox.html (accessed November 12, 2022).

[51] G.R. Li, B.W. Lv, G.J. Yang, W.X. Zhang, C.X. Li, C.J. Li, Relationship between lamellar structure and elastic modulus of thermally sprayed thermal barrier coatings with intra-splat cracks, J. Therm. Spray. Technol. 24 (2015) 1355–1367, https://doi.org/10.1007/S11666-015-0292-5.

[52] T. Shimonosono, T. Ueno, Y. Hirata, Mechanical and thermal properties of porous yttria-stabilized zirconia, J. Asian Ceram. Soc. 7 (2018) 20–30, https://doi.org/10.1080/21870764.2018.1547248.

[53] P. Bednarz, Finite Element Simulation of Stress Evolution in Thermal Barrier Coating Systems, PhD Thesis, RWTH Aachen University, 2006.

[54] H.X. Zhu, N.A. Fleck, A.C.F. Cocks, A.G. Evans, Numerical simulations of crack formation from pegs in thermal barrier systems with NiCoCrAlY bond coats, Mater. Sci. Eng.: A 404 (2005) 26–32, https://doi.org/10.1016/J.MSEA.2005.05.033.

[55] H. Dong, G.J. Yang, H.N. Cai, H. Ding, C.X. Li, C.J. Li, The influence of temperature gradient across YSZ on thermal cyclic lifetime of plasma-sprayed thermal barrier coatings, Ceram. Int 41 (2015) 11046–11056, https://doi.org/10.1016/J.CERAMINT.2015.05.049.